Nonlinear Dyn (2020) 101:2107–2129
https://doi.org/10.1007/s11071-020-05931-w

ORIGINAL PAPER

Dynamic analysis of piezoelectric energy harvester under combination parametric and internal resonance: a theoretical and experimental study

Anshul Garg · **Santosha K. Dwivedy**

Received: 1 February 2020 / Accepted: 29 August 2020 / Published online: 19 September 2020
© Springer Nature B.V. 2020

Abstract In this work, theoretical and experimental analysis of a piezoelectric energy harvester with parametric base excitation is presented under combination parametric resonance condition. The harvester consists of a cantilever beam with a piezoelectric patch and an attached mass, which is positioned in such a way that the system exhibits 1:3 internal resonance. The generalized Galerkin's method up to two modes is used to obtain the temporal form of the nonlinear electromechanical governing equation of motion. The method of multiple scales is used to reduce the equations of motion into a set of first-order differential equations. The fixed-point response and the stability of the system under combination parametric resonance are studied. The multi-branched non-trivial response exhibits bifurcations such as turning point and Hopf bifurcations. Experiments are performed under various resonance conditions. This study on the parametric excitation along with combination and internal resonances will help to harvest energy for a wider frequency range from ambient vibrations.

Keywords Nonlinear dynamics · Piezoelectric energy harvester · Internal resonance · Combination parametric resonance · Bifurcation · Method of multiple scales

A. Garg (✉)· S. K. Dwivedy
Department of Mechanical Engineering, Indian Institute of Technology Guwahati, Assam 781039, India
e-mail: anshul.sv@gmail.com

S. K. Dwivedy
e-mail: dwivedy@iitg.ac.in

1 Introduction

The low-powered microelectronic systems [1], which are used as sensors and actuators, need to be self-reliant in the energy front for remote operations. The ambient kinetic energy available from sources such as winds and vibrating structures can be utilized to convert into electricity by several mechanisms. These transduction mechanisms [2,3] are piezoelectric, electromagnetic, and electrostatic, which are extensively utilized for energy harvesting purposes mostly in the linear range of oscillations. The combination of these three transduction mechanisms is also explored as hybrid energy harvesters [4–6]. Among them, the piezoelectric-based energy harvesting has been the most attractive one due to its energy extracting capabilities over a wide range of available frequencies. Researchers started with linear vibration-based harvesters [7,8], but the limitations of having limited frequency bandwidth and very few resonance conditions lead to shift their focus on nonlinear vibration-based harvesters [9–17]. The term bandwidth is defined as the range of frequency that is available for energy transduction. Wider bandwidth means a higher range of ambient frequency over which energy transfer is possible. Rich dynamical behavior (e.g., multiple resonances, bifurcation, internal resonance, and chaos) [18,19] of nonlinear vibration-based harvesting systems brings several advantages in power harvesting

capabilities as the ambient vibration contains a wide range of frequencies and hence outperforms the linear harvesters. There has been an enormous amount of literature available where piezoelectric energy harvester (PEH) with harmonic excitation (direct) has been analyzed. Very few researchers analyzed or developed the parametrically excited PEH systems even though in the case of parametric excitation [20–22] a small input amplitude can create large deflection.

Daqaq et al. [23] was the first to investigate a nonlinear parametrically excited cantilever beam as energy harvester considering lumped parameter model with single-mode approximation. The broadband characteristics of the harvester are found to be affected by the coupling coefficient and load resistance. It is also observed that a critical amplitude of excitation should always be maintained for the nontrivial response. Abdelkefi et al. [24] developed a distributed parameter model of parametrically excited nonlinear PEH system, which consists of a cantilever beam with a tip mass. Jia et al. [25] shown that when it comes to power harvesting, the parametric resonance is found to be superior over ordinary resonance. In this case, one has to overcome some limitations such as a requirement of a critical amplitude of excitation and requirement of initial push for a nontrivial solution. Other recent notable works where parametric excitation is used in PEH systems are referenced here [26–28]. Nonlinearity brings an interesting dynamic phenomenon, i.e., internal resonance (IR) in multimode systems. While in the case of linear systems, the different modes can be excited separately by adjusting the external excitation, in nonlinear systems, coupling among different modes is possible [29–31]. Internal resonance arises when the modal frequencies are in integer relationship with each other. For example, if the second modal frequency is near twice the first-mode frequency, one may observe 1:2 internal resonance condition. In other words, this commensurable or nearly commensurable frequency ratios [32] causes the mode coupling phenomenon [33] and energy transfer takes place between participating modes of the system. This leads to periodic, quasi-periodic, and chaotic responses [34,35]. Such responses attracted the scientific community from time to time and inspired them to apply internal resonance condition in multidimensional interconnected systems for a large number of application fields. In order to seek better performance in the field of PEH, few recently developed systems [36–40] incorporated the internal resonance condition of 1:2. Similarly, Yan and Hajj [41] investigated an autoparametric vibration-based PEH for enhanced frequency bandwidth where the frequency ratio of the beam to the base structure is taken as 1:2 that causes the beam motion. A hybrid PEH system with internal resonance (2:1) is explored by Yang and Towfighian [6], where an axially movable magnet-based bistable configuration is analyzed. It is observed that large magnetization moment and closely placed magnets lead to wide bandwidth. In all these internal resonances-based PEH systems, an auxiliary system is attached to the main system in such a way that the combined system exhibits internal resonance. To the best of the authors' knowledge, no attempt has been made where a compact system (without auxiliary system) with internal resonance is developed as a PEH system. As mentioned before, few researchers have considered parametrically excited PEH with principal parametric resonance conditions; none of them has explored the PEH system with a combination parametric resonance condition. As superposition rule is not valid for nonlinear systems, one cannot extend the results of principal parametric resonance condition for combination parametric resonance condition. Hence, the study of a nonlinear PEH subjected to combination parametric resonance condition is attempted in this work.

In the present work, an energy harvesting system consists of a harmonic base excited vertical cantilever beam with bimorph piezoelectric patches considered for dynamic analysis. To achieve an internal resonance of 1:3, a mass is attached at a particular position along the beam. In this case, the frequency of external excitation is taken as the sum of the first two modal frequencies, and hence, the system is subjected to combination parametric resonance of the sum type. In the present work, the governing spatiotemporal electromechanical equation of motion is derived using extended Hamilton's principle and it is discretized to its temporal form by using generalized Galerkin's method. The method of multiple scales (MMS) is used to reduce the nonlinear governing differential equations of motion into first-order differential equations to obtain the steady-state response and output voltage. The dynamics of the system are analyzed for combination parametric with internal resonance condition of 1:3 in order to achieve a wide frequency bandwidth. It may be noted that authors have studied the PEH with principal parametric resonance condition with 1:3 internal resonance in their earlier work [42].

2 Modeling and governing equation

A vertical slender cantilever beam-based energy harvester (Fig. 1) having length L and attached mass m at an arbitrary position d from the base with bimorph piezoelectric patches of length L_p ($L_p = L_2 - L_1$) is subjected to a harmonic base excitation $z(t) = z_0 \cos(\Omega t)$. Considering an arbitrary point along the longitudinal direction of the beam, at a curvilinear distance s from the base, the transverse and axial displacements are expressed as $v(s,t)$ and $u(s,t)$, respectively. Due to large deflection, the displacement–curvature relation of the beam is considered as nonlinear. The Hamilton's principle $\int_{t_1}^{t_2} \hat{\delta}\,(T - U + W_{\text{nc}})\,\mathrm{d}t$ is used to find the governing equation of motion of the beam-based energy harvester. The kinetic energy (T) and potential energy (U) of the harvester are expressed as:

$$T = \frac{1}{2}\int_0^L \rho^*(s)\left(\dot{u}(s,t)^2 + \dot{v}(s,t)^2\right)\mathrm{d}s + \frac{1}{2}J_0\dot{\varphi}(d)^2 \tag{1}$$

$$U = \frac{1}{2}\int_0^L E_b I_b \varphi'(s)^2\,\mathrm{d}s - \int_0^L \rho^*(s) g\, u(s,t)\,\mathrm{d}s. \tag{2}$$

Here, $\rho^*(s) = [\rho + m\delta\,(s-d)]$, $\rho = \rho_b A_b + 2\left(H_{L_1} - H_{L_2}\right)\rho_p A_p$, δ, J_0, φ, and $E_b I_b$, respectively, denotes the mass per unit length, Dirac delta function, polar moment of inertia of the attached mass m, rotation angle of the beam from the x-axis, and flexural rigidity of the beam. Also, ρ_b, ρ_p, A_b, A_p, and H are mass density of beam, mass density of patch, area of cross section of beam, area of cross section of patch, and Heaviside step function, respectively. Further, following similar to the work of Zavodney and Nayfeh [43] the relation between the lateral and longitudinal displacement is considered to be governed by the inextensibility condition, which can be expressed as follows:

$$u(s,t) = \left(\tfrac{1}{2}\right)\int_0^s \left\{v'(\xi,t)\right\}^2 \mathrm{d}\xi + z(t). \tag{3}$$

By observing the deflected beam geometry, the relation between the angle of rotation $\varphi(s)$ and transverse deflection $v(s,t)$ is defined as $\sin\varphi = v'$ and $\cos\varphi = (1 - v'^2)^{1/2}$. As per the Euler–Bernoulli beam theory, the curvature $\kappa(s,t)$ is written as follows:

$$\kappa(s,t) = \frac{\partial\varphi(s)}{\partial s} = \frac{v''}{\cos\varphi} = \frac{v''}{\sqrt{1 - v'^2}} \approx v''\left(1 + \frac{1}{2}v'^2\right). \tag{4}$$

The non-conservative virtual work done W_{nc} involves the work done in dissipation of energy by viscous force W_{d} and electrical forces W_{ele} [44] which is because of piezoelectric elements attached with the beam system. The virtual work done W_{nc} ($W_{\text{nc}} = W_{\text{d}} + W_{\text{ele}}$) is expressed as follows:

$$\hat{\delta} W_{\text{nc}} = -\int_0^L c\dot{v}(s,t)\delta v\,\mathrm{d}s - \int_0^L \left(H_{L_1} - H_{L_2}\right) M_{\text{ele}}(s,t)\delta\kappa(s)\mathrm{d}s. \tag{5}$$

The total moment M_{ele} due to piezoelectric patches is expressed as follows:

$$M_{\text{ele}} = \int_{-h_2}^{-h_1} d_{31}E_p b_p E_e\, y\,\mathrm{d}y + \int_{h_1}^{h_2} d_{31}E_p b_p(-E_e)\, y\,\mathrm{d}y.$$

Here,

$$E_e = \frac{\bar{V}(t)}{t_p};\ \ h_1 = \tfrac{1}{2}t_b;\ \ h_2 = \tfrac{1}{2}t_b + t_p.$$

Here, d_{31}, E_p, b_p, t_p, E_e, and $\bar{V}$ are piezoelectric strain coefficient, Young's modulus of piezoelectric patch, patch width, patch thickness, electric field, and voltage across the electrodes, respectively. Further, following the work of Zavodney and Nayfeh [43], Erturk and Inman [44] and Kar and Dwivedy [45], the nonlinear coupled electromechanical governing equation of motions which represents the dynamics of the PEH can be expressed as follows:

$$\begin{aligned}&\left[\rho_b A_b + 2\left(H_{L_1} - H_{L_2}\right)\rho_p A_p + m\delta(s-d)\right]v_{tt} + cv_t\\ &\quad + \left(E_b I_b + 2\left(H_{L_1} - H_{L_2}\right)E_p I_p\right)\\ &\quad \times\left[v_{ssss} + \{v_s(v_s v_{ss})_s\}_s\right]\\ &\quad -\left[(J_0\delta(s-d))(v_s)_{tt}\right]_s - (Nv_s)_s - H_{ss}\eta\bar{V} = 0.\end{aligned} \tag{6}$$

Here,

$$\eta = \frac{e_{31}b_p}{t_p}\left[\left(t_p + \tfrac{1}{2}t_b\right)^2 - \tfrac{1}{4}t_b{}^2\right],$$
$$A_b = b_b t_b,\ \ A_p = b_p t_p,$$
$$H = H_{L_1} - H_{L_2} = H(s - L_1) - H(s - L_2),$$

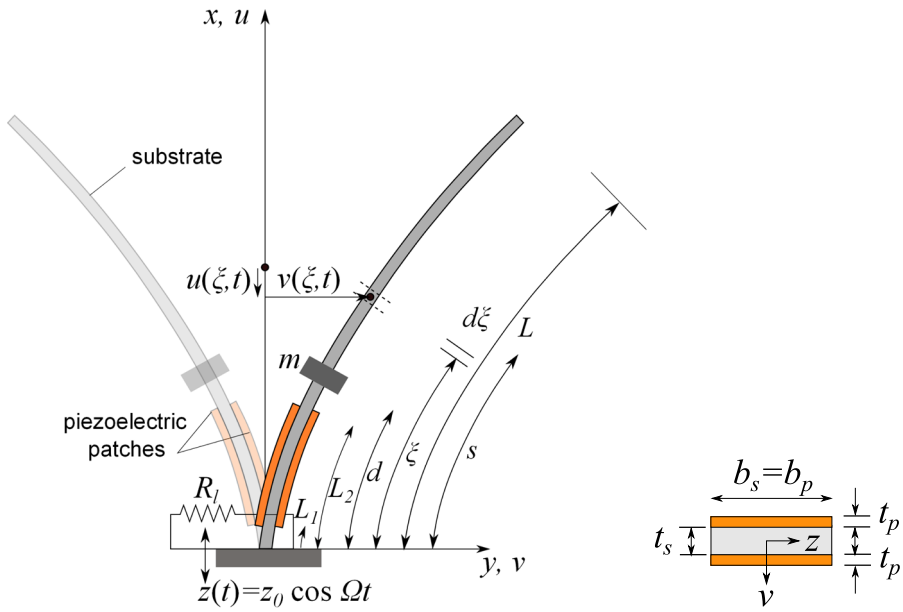

Fig. 1 **a** Schematic diagram of piezoelectric-based energy harvester, **b** cross section

$$e_{31} = d_{31}E_p,$$
$$I_p = \tfrac{1}{3}b_p\left[(t_p + \tfrac{1}{2}t_b)^3 - \tfrac{1}{8}t_b{}^3\right],\ \ I_b = \tfrac{1}{12}b_b t_b{}^3,$$
$$L_p = L_2 - L_1$$
$$N = \int_s^L \left[\rho_b A_b + 2H\rho_p A_p + m\delta(s-d)\right] \times \left(\frac{1}{2}\int_0^\xi (v_s^2)_{tt}\mathrm{d}\eta + (z_{tt} - g)\right)\mathrm{d}\xi$$

where subscript 'p' is used to denote terms related to Macro Fiber Composite (MFC) and $(\ )_s$, $(\ )_t$ denotes the differentiation w.r.t curvilinear coordinate 's', i.e., $\frac{d(\ )}{ds}$ and time $\frac{d(\ )}{dt}$, respectively. Term N denotes the longitudinal load at 's'. The electric circuit equation in bimorph configuration (with parallel connection, Fig. 2) can be obtained by applying the Gauss's law [44,46]

$$\frac{\mathrm{d}Q(t)}{\mathrm{d}t} = \frac{\mathrm{d}}{\mathrm{d}t}\int_{A_p} \mathbf{D}\,.\,\mathbf{n}\ \mathrm{d}A_p. \tag{7}$$

Here, Q, $\mathbf{D}$, and $\mathbf{n}$ denote the developed electric charge, electric displacement vector, and outward normal to the surface. The electric displacement vector ($\mathbf{D}$) in terms of axial stress (σ_p), dielectric permittivity component $\hat{e}$, and generated electric field (E_e) in the present case is defined by the following constitutive relation:

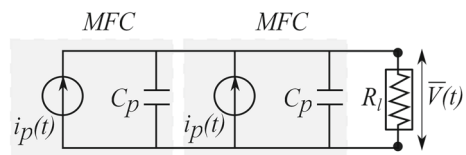

Fig. 2 Electric circuit in parallel connection

$$D_3 = d_{31}\sigma_p + \hat{e}\,E_e. \tag{8}$$

Here, $\sigma_p = E_p\epsilon_p - e_{31}E_e,\ \epsilon_p = -y\kappa(s,t)$.

By substituting Eq. (8) into Eq. (7), the circuit equation becomes as follows:

$$C_p\bar{V}_t + \frac{1}{2R_l}\bar{V} - i(t) = 0. \tag{9}$$

Here, $i(t) = -e_{31}t_{pc}b_p\int_{L_1}^{L_2}(v_{ss})_t\mathrm{d}s,\ C_p = \frac{\hat{e}b_pL_p}{t_p}$. The four boundary conditions at fixed and free ends are represented as follows:

$$v(0,t) = 0,\ \ v_s(0,t) = 0,\ \ v_{ss}(L,t) = 0,\ \ v_{sss}(L,t) = 0.$$

At the fixed end displacement, slope is zero, and at the free end the bending moment and shear forces are zero. By considering the two-mode approximation in the Galerkin's method, the transverse displacement $v(s,t)$ is represented by a scaling factor r, time modulation

$q_n(t)$, and shape function $\psi_n(s)$ of the beam system as $v(s,t) = \sum_{n=1}^{2} r\ \psi_n(s)\ q_n(t)$. After nondimensionalizing, the nonlinear coupled electromechanical temporal governing equations of motion for two modes ($n = 1,\ 2$) are as follows:

$$\ddot{q}_n + 2\epsilon\zeta_n\dot{q}_n + \omega_n^2 q_n + \epsilon \sum_{k,l,m=1}^{2} \{\alpha_{klm}^n q_k q_l q_m + \beta_{klm}^n q_k \dot{q}_l \dot{q}_m + \gamma_{klm}^n q_k q_l \ddot{q}_m\} + \epsilon\eta_n V = \epsilon \sum_{m=1}^{2} F_{nm}\cos(\phi\tau) q_m \tag{10}$$

$$\dot{V}(\tau) + \chi V(\tau) + \left(\sum_{n=1}^{2} \frac{e_{31} t_{pc} b_p}{L} \frac{r}{C_p r_v} \int_0^1 \psi_{nxx}(x)\mathrm{d}x\right)\dot{q}_n = 0. \tag{11}$$

Here,

$$x = \frac{s}{L},\ \beta = \frac{d}{L},\ \tau = \theta_1 t,\ \omega_n = \frac{\theta_n}{\theta_1},\ \lambda = \frac{r}{L},$$

$$\mu = \frac{m}{\rho L},\ J = \frac{J_0}{\rho L r^2}, t_{pc} = (t_p + t_b)/2,$$

$$\phi = \frac{\Omega}{\theta_1},\ \zeta_n = \zeta_n^* \frac{\nu}{\epsilon},\ \Gamma = \frac{z_0}{z_r},\ F_{nm} = F_{nm}^* \frac{\Gamma}{\epsilon},$$

$$\eta_n = \frac{-\eta r_v}{\rho \hbar_n \theta_1^2 r \epsilon L^2} \int_0^1 \{\delta_x(x) - \delta_x(x-1)\}\ \psi_n(x)\mathrm{d}x,$$

$$\chi = \frac{1}{2C_p\theta_1 R_l},\ \bar{K}_n = \frac{e_{31} t_{pc} b_p}{L} \int_0^1 \psi_{nxx}(x)\mathrm{d}x,$$

$$K_n = \frac{\bar{K}_n r}{C_p r_v},\ r_v = \frac{\bar{V}}{V} = \frac{\bar{K}_n r}{C_p}$$

where $\dot{(\ )} = \frac{d(\ )}{d\tau}$. Here, the damping, geometric and inertial nonlinearities, electromechanical coupling and excitation terms are small and hence considered of the order of ϵ (bookkeeping parameter). The coefficients of linear (ζ_n, θ_n), nonlinear (α_{klm}^n, β_{klm}^n, γ_{klm}^n), coupling (η_n), and forcing term (F_{nm}), which appear in the governing Eqs. (10) and (11), are defined in "Appendix A." By observing the RHS term of Eq. (10), the time-varying forcing term appears as a parameter [21], which is a typical characteristic of parametrically excited systems. It may be noted that in the absence of piezo-patches with single-mode approximation, the equation of motion of the system reduces to that of the model investigated theoretically and experimentally by Zavodney and Nayfeh [43]. Also, with two-mode approximation, the governing equation of motion without piezoelectric patches reduces to that of Kar and Dwivedy [45]. The present mathematical model accommodates the variation in the position of piezoelectric patches. A similar approach is adopted by Yan and Hajj [41] in the development of the autoparametric PEH system, where tip mass is used.

3 Solution of the temporal equation

A uniform first-order approximate analytical solution of Eqs. (10) and (11) is obtained by using the standard method of multiple scales (MMS). Though in the present case combination parametric resonance is studied, in Zavodney and Nayfeh [43], and Kar and Dwivedy [45], principal parametric resonance conditions were discussed. In the work by Dwivedy and Kar [47] and Dwivedy and Kar [34], the combinational resonance cases were discussed where the dynamic analysis of the beam is studied. However, in the present work, the nonlinear electromechanical system is explored as an energy harvester. The time dependence is expressed into multiple timescales as $T_n = \epsilon^n\tau;\ n = 0,\ 1,\ 2,\ldots$, and the time derivatives can be $\frac{d}{d\tau} = D_0 + \epsilon D_1 + O(\epsilon^2)$, $\frac{d^2}{d\tau^2} = D_0^2 + 2\epsilon D_0 D_1 + O(\epsilon^2)$ where $D_i = \frac{\partial}{\partial T_i}$. The solution of the system (q_n, V) can be expanded in the following form:

$$q_n(\tau;\epsilon) = q_{n0}(T_0, T_1) + \epsilon q_{n1}(T_0, T_1) + O(\epsilon^2) \tag{12}$$

$$V(\tau;\epsilon) = V_0(T_0, T_1) + \epsilon V_1(T_0, T_1) + O\left(\epsilon^2\right). \tag{13}$$

Substituting Eqs. (12) and (13) into Eqs. (10) and (11) and further equating the coefficient involving the terms of ϵ^0 and ϵ^1 to zero yields the set of equations in different order of ϵ

$O(\epsilon^0)$:

$$\begin{aligned} &D_0^2 q_{n0} + \omega_n^2 q_{n0} = 0; \\ &D_0 V_0 + \chi V_0 = -K_1 D_0 q_{10} - K_2 D_0 q_{20} \end{aligned} \tag{14}$$

$O(\epsilon^1)$:

$$\begin{aligned} D_0^2 q_{n1} + \omega_n^2 q_{n1} &= -2\zeta_n D_0 q_{n0} - 2D_0 D_1 q_{n0} \\ &+ \sum_{n,m=1}^{2} F_{nm} q_{m0}\cos\phi\tau - \eta_n V_0 \\ &- \sum_{klm} \left(\alpha_{klm}^n q_{k0} q_{l0} q_{m0} + \beta_{klm}^n q_{k0} D_0 q_{l0} D_0 q_{m0} \right. \\ &\left. + \gamma_{klm}^n q_{k0} q_{l0} D_0^2 q_{m0}\right) \\ D_0 V_1 + \chi V_1 &= -D_0 V_0 - K_1 (D_0 q_{11} + D_1 q_{10}) \end{aligned}$$

$$-K_2\left(D_0 q_{21}+D_1 q_{20}\right). \tag{15}$$

The solution of differential equations (Eq. (14)) of $O(\epsilon^0)$ is expressed as

$$\begin{aligned} q_{n0} &= A_n(T_1)\exp(i\omega_n T_0)+cc,\\ V_0 &= -\sum_{n=1}^{2} K_n Z_n A_n(T_1)\exp(i\omega_n T_0)+cc. \end{aligned} \tag{16}$$

Here, cc is the complex conjugate of the preceding terms and is an unknown complex function to be determined later. By substituting Eq. (16) into Eq. (15), the following secular and near secular terms for first two modes ($n=1,\ 2$) are obtained which should be eliminated for finite amplitude response of the system:

$$\begin{aligned} n=1:\ & \frac{1}{2}\mathrm{e}^{i(\phi-\omega_2)T_0}F_{12}\bar{A}_2 - Q_1^* A_2\bar{A}_1^2\mathrm{e}^{i(\omega_2-2\omega_1)T_0}\\ & + e^{i\omega_1 T_0}\Bigg[-2i\omega_1\left(\zeta_1 A_1 + A_1{}'\right)+\eta_1 K_1 Z_1 A_1\\ & -\sum_{j=1}^{2}\alpha_{e1j}A_j\bar{A}_j A_1\Bigg]=0 \end{aligned} \tag{17}$$

$$\begin{aligned} n=2:\ & \frac{1}{2}\mathrm{e}^{i(\phi-\omega_1)T_0}F_{21}\bar{A}_1 - Q_2^*\mathrm{e}^{3i\omega_1 T_0}A_1{}^3\\ & + e^{i\omega_2 T_0}\Bigg[-2i\omega_2(\zeta_2 A_2 + A_2{}')+\eta_2 K_2 Z_2 A_2\\ & -\sum_{j=1}^{2}\alpha_{e2j}A_j\bar{A}_j A_2\Bigg]=0 \end{aligned} \tag{18}$$

Equations (17) and (18) are obtained by considering a particular case of combination resonance of sum type when the frequency of external excitation is nearly commensurate to the sum of first two natural frequencies of the system, i.e., $\phi\approx\omega_1+\omega_2$. Also, 1:3 internal resonance condition is considered here by taking $\omega_2\approx 3\omega_1$. Here, terms Q_1^* and Q_2^* are the functions of $\alpha^n_{klm}, \beta^n_{klm}, \gamma^n_{klm}$ and ω_n which are defined in "Appendix A." To express the nearness of ϕ to that of $\omega_1+\omega_2$ and ω_2 to that of ω_1, the detuning parameters σ_1 and σ_2 are introduced as follows:

$$\begin{aligned} \omega_2 &= 3\omega_1+\epsilon\sigma_2,\\ \phi &= 4\omega_1+\epsilon\sigma_1=\omega_1+\omega_2+\epsilon(\sigma_1-\sigma_2). \end{aligned} \tag{19}$$

The complex function $A_n(T_1)$ is expressed into its polar form as $A_n(T_1)=\frac{1}{2}a_n(T_1)e^{i\vartheta_n(T_1)}$, where amplitude $a_n(T_1)$ and phase $\vartheta_n(T_1)$ are slowly varying functions of timescale T_1. Now by using this polar form in Eqs. (17) and (18) and eliminating the secular term (the coefficient of $e^{i\omega_n T_0}$) to find the bounded solution, one obtains the following reduced equations:

$$2\omega_1 a_1{}' = -2\omega_1\zeta_1 a_1+\frac{1}{2}\{F_{12}a_2\sin(\gamma_1+\gamma_2)\}-\frac{1}{4}Q_1^* a_2 a_1{}^2\sin(3\gamma_1-\gamma_2)+\Pi_a a_1 \tag{20}$$

$$2\omega_1 a_1\gamma_1{}' = 0.5\omega_1 a_1\sigma_1+\frac{1}{2}\{F_{12}a_2\cos(\gamma_1+\gamma_2)\}-\frac{1}{4}\sum_{j=1}^{2}\alpha_{e1j}a_j{}^2 a_1-\frac{1}{4}Q_1^* a_2 a_1{}^2\cos(3\gamma_1-\gamma_2)+\Pi_b a_1 \tag{21}$$

$$2\omega_2 a_2{}' = -2\omega_2\zeta_2 a_2+\frac{1}{2}F_{21}a_1\sin(\gamma_2+\gamma_1)-\frac{1}{4}Q_2^* a_1{}^3\sin(\gamma_2-3\gamma_1)+\Pi_c a_2 \tag{22}$$

$$\begin{aligned} 2\omega_2 a_2\gamma_2{}' = {}& \omega_2 a_2(1.5\sigma_1-2\sigma_2)+\frac{1}{2}F_{21}a_1\cos(\gamma_2+\gamma_1)-\frac{1}{4}\sum_{j=1}^{2}\alpha_{e2j}a_j{}^2 a_2-\frac{1}{4}Q_2^* a_1{}^3\cos(\gamma_2-3\gamma_1)\\ & +\Pi_d a_2. \end{aligned} \tag{23}$$

Here,

$$\begin{aligned} \Pi_a &= \frac{K_1\eta_1\chi\omega_1}{(\chi^2+\omega_1{}^2)},\quad \Pi_b=\frac{K_1\eta_1\omega_1{}^2}{(\chi^2+\omega_1{}^2)},\\ \Pi_c &= \frac{K_2\eta_2\chi\omega_2}{(\chi^2+\omega_2{}^2)},\quad \Pi_d=\frac{K_2\eta_2\omega_2{}^2}{(\chi^2+\omega_2{}^2)}\\ Z_n &= \frac{\omega_n{}^2+i\chi\omega_n}{(\chi^2+\omega_n{}^2)},\quad \gamma_1=-\vartheta_1+0.25\sigma_1 T_1,\\ \gamma_2 &= -\vartheta_2+0.75\sigma_1 T_1-\sigma_2 T_1. \end{aligned}$$

The stability of nontrivial state can be obtained by perturbing Eqs. (20)–(23). But for the trivial state, the stability cannot be determined by perturbing Eqs. (21)

and (23) as the perturbation will not contain the term $\Delta\gamma_1'$ and $\Delta\gamma_2'$ due to the presence of coupled term $a_1\gamma_1'$ and $a_2\gamma_2'$. By using the transformation $p_i = a_i \cos\gamma_i$; $q_i = a_i \sin\gamma_i$; $i = 1, 2$, the following normalized reduced equations in Cartesian form are obtained:

$$p_1' = \frac{-1}{2\omega_1}\left[\begin{array}{l} 2\omega_1\zeta_1 p_1 + \frac{1}{2}\omega_1\sigma_1 q_1 - \frac{1}{2}F_{12}q_2 + \frac{1}{4}Q_1^*\left\{q_2\left(q_1^2 - p_1^2\right) + 2p_1p_2q_1\right\} \\ -\frac{1}{4}\sum_{j=1}^{2}\alpha_{e1j}q_1\left(p_j^2 + q_j^2\right) - \Pi_a p_1 + \Pi_b q_1 \end{array}\right] \tag{24}$$

$$q_1' = \frac{-1}{2\omega_1}\left[\begin{array}{l} 2\omega_1\zeta_1 q_1 + \frac{1}{2}\omega_1\sigma_1 p_1 - \frac{1}{2}F_{12}p_2 + \frac{1}{4}Q_1^*\left\{p_2\left(p_1^2 - q_1^2\right) + 2p_1q_1q_2\right\} \\ +\frac{1}{4}\sum_{j=1}^{2}\alpha_{e1j}p_1\left(p_j^2 + q_j^2\right) - \Pi_b q_1 - \Pi_a p_1 \end{array}\right] \tag{25}$$

$$p_2' = \frac{-1}{2\omega_2}\left[\begin{array}{l} 2\omega_2\zeta_2 p_2 - \omega_2\left(2\sigma_2 - 1.5\sigma_1\right)q_2 - \frac{1}{2}F_{21}q_1 - \frac{1}{4}Q_2^*\left\{q_1\left(3p_1^2 - q_1^2\right)\right\} \\ -\frac{1}{4}\sum_{j=1}^{2}\alpha_{e2j}q_2\left(p_j^2 + q_j^2\right) - \Pi_c p_2 + \Pi_d q_2 \end{array}\right] \tag{26}$$

$$q_2' = \frac{-1}{2\omega_2}\left[\begin{array}{l} 2\omega_2\zeta_2 q_2 + \omega_2\left(2\sigma_2 - 1.5\sigma_1\right)p_2 - \frac{1}{2}F_{21}p_1 + \frac{1}{4}Q_2^*\left\{p_1\left(p_1^2 - 3q_1^2\right)\right\} \\ +\frac{1}{4}\sum_{j=1}^{2}\alpha_{e2j}p_2\left(p_j^2 + q_j^2\right) - \Pi_c q_2 - \Pi_d p_2 \end{array}\right]. \tag{27}$$

Here, Newton's method is used to find the nontrivial fixed-point responses of the system. Further to find the stability of the obtained fixed-point responses, the above reduced modulation equations [Eqs. (24)–(27)] are then perturbed to obtain the following equations:

$$\left\{\Delta p'_1, \Delta q'_1, \Delta p'_2, \Delta q'_2\right\}^T = [J]\{\Delta p_1, \Delta q_1, \Delta p_2, \Delta q_2\}^T \tag{28}$$

where Δ, superscript T, and matrix $[J]$ denote the perturbation to the fixed point, the transpose, and the Jacobian matrix, respectively. The stability and bifurcation of the fixed-point response of the system can be obtained by finding the eigenvalue of the Jacobian $[J]$. It may be noted that the solutions having eigenvalues with negative real parts are stable solutions and those with positive real parts are unstable solutions. One can obtain the steady-state deflection of the beam v, output voltage V, and power P, by using the following expressions:

$$v(s,\tau) = \sum_{n=1}^{2} r\ \psi_n(s)a_{n0}\cos(\omega_n\tau + \vartheta_n) \tag{29}$$

$$V(\tau) = \sum_{n=1}^{2} r_v\ K_n\frac{\omega_n}{\sqrt{\chi^2+\omega_n^2}}a_{n0}\cos(\omega_n\tau + \vartheta_n + \delta_n) \tag{30}$$

$$P = \frac{1}{R_l}\left(\sum_{n=1}^{2} r_v\ K_n\frac{\omega_n}{\sqrt{\chi^2+\omega_n^2}}a_{n0}\right)^2. \tag{31}$$

Here, $\delta_n = \tan^{-1}\left(\frac{\chi}{\omega_n}\right)$.

4 Results and discussion

This section deals with the parametric study of energy harvester for combination parametric and 1:3 internal resonance condition using the reduced equations developed in the previous section. The material and geometric properties of the substrate and piezoelectric patch considered in this work are given in Table 1. The trivial state instability regions are obtained by finding the eigenvalues of the Jacobian matrix $[J]$ [Eqs. (24)–(27)] by substituting $p_1 = p_2 = q_1 = q_2 = 0$. Figure 3a shows the trivial state instability regions with variation in load resistance (R_l) for damping parameter $\nu = 0.0005$. In this figure, the abbreviation S and US denote the stable and unstable trivial state regions. It may be noted that there exists a critical value of the nondimensional amplitude of excitation Γ_{crit} below which for all the frequency range, the trivial state remains stable. Hence, there will be no transverse vibration of the beam system and hence no power generation is possible. Further, it may be observed (Fig. 4) that in the US region, branches of nontrivial fixed-point response and periodic responses are possible and hence for this trivial state unstable region, the energy harvesting is possible. As the load resistance (R_l) increases, insta-

Table 1 Material and geometric properties of substrate and piezoelectric patches

Property	Piezo-patch	Substrate
Young's modulus, GPa	$E_p = 15.86$	$E_b = 130$
Density, kg m^{-3}	$\rho_p = 5440$	$\rho_b = 1794$
Length, m	$L_p = 7.6 \times 10^{-2}$	$L_b = 32 \times 10^{-2}$
Width, m	$b_p = 1.8 \times 10^{-2}$	$b_b = 1.8 \times 10^{-2}$
Height, m	$t_p = 1.25 \times 10^{-4}$	$t_b = 2.5 \times 10^{-4}$
Permittivity, nF m^{-1}	$\hat{e} = 19.36$	–
Piezoelectric constant, Cm^{-2}	$e_{31} = -19.84$	–
Subscript	p:piezo	b:beam

bility regions shifted slightly toward the higher frequency side. For example, the critical value of Γ above which trivial state loses its stability gets increased from $\Gamma = 0.55$ ($\phi = 4.026$ for $R_l = 0.5$ kΩ) to $\Gamma = 3.55$ ($\phi = 4.033$ for $R_l = 10$ kΩ). In Fig. 4, the time response for three data points $O_1(\phi = 3.95,\ \Gamma = 6)$, $O_2(\phi = 4.00,\ \Gamma = 6)$ and $O_3(\phi = 4.10,\ \Gamma = 6)$ shows that there is no voltage generation in the region marked with S and only the region marked with US is available for harvesting. Further, it may be noted that for a particular value of Γ, as the unstable range increases with an increase in R_l, suitable value of R_l may be taken depending on the requirement of the available amplitude and frequency range of the ambient vibration source for the PEH applications.

Figure 3b shows the instability region plot in $\Gamma - \phi$ plane, with variation in damping parameter, $\nu = 0.0005, 0.001, 0.005, 0.01$ for a load resistance of $R_l = 0.5$ kΩ. As the nondimensional damping parameter ν increases, the stability region shifts toward higher values of Γ. Hence, similar to the previous case, here with an increase in ν, the critical value of Γ above which the PEH can operate becomes higher. In Fig. 5, frequency response curves are plotted for the system parameters $\nu = 0.0005$, $\Gamma = 4$, $R_l = 0.5$ kΩ along with variation of voltage and power with respect to the frequency of the excitation ϕ. In all the frequency response plots, the stable solutions are shown in black color and the unstable solutions are shown in blue color. It may clearly be observed from Figs. 3, 4, and 5 that the trivial state loses its stability by Hopf bifurcation (left HB_T^L) at $\phi = 3.99$ and remain unstable up to $\phi = 4.057$ (right HB_T^R). Among all the nontrivial branches, only two are stable (as shown by black color) and loses its stability by Hopf bifurcation (HB) at $\phi = 3.970$ (left HB_{NT}^L) and $\phi = 4.007$ (right HB_{NT}^R), respectively. If one sweeps down the frequency from $\phi > 4.057$, as the stable trivial state loses its stability at right HB point ($\phi = 4.057$), the response will jump to the nontrivial stable branch. For further sweeping down the frequency ϕ, the nontrivial response remains stable in the considered range and one may observe a decrease in amplitude, voltage, and power. Further, sweeping up the frequency ϕ, the nontrivial response remains stable and an increase in amplitude, voltage, and power is observed. For example, for a positively tuned system (i.e., $\sigma_1 > 0$) when $\phi = 4.1$, the voltage and power are 1.8 V and 6.3 mW, respectively. Similarly, for $\phi = 4.2$, the voltage and power increase to 2.46 V and 12.1 mW and negatively tuned cases such as $\phi = 3.5$, the voltage and power are found to be 1.03 V and 2.08 mW, respectively. So, depending on the applications, the harvester may be operated at a particular frequency to obtain the required voltage and power.

As four state vectors (a_1, a_2, γ_1, γ_2) are there to represent the response of the system, it is difficult to show the basin of attraction. Hence, keeping $\gamma_1 = 3.78$ and $\gamma_2 = 4.97$, which are obtained from the frequency response plots, the basin of attraction is plotted in $a_1 - a_2$ plane at frequency of excitation, $\phi = 3.7$. To achieve this, a grid of 30×30 is considered in $a_1 - a_2$ plane. So, taking 900 initial conditions the time responses have been plotted which are shown in Fig. 6. It may clearly be observed that few points marked in this figure are matching with the response amplitude present in the frequency plot shown in Fig. 5a, b. In addition to these fixed-point responses, some periodic responses are also observed which are shown in Fig. 7 due to the existence of Hopf bifurcation. Then, the basin of attraction is plotted by marking all the grid points (▲,▼,▼) going to the same final equilibrium points (•,•,•) in same color as shown in Fig. 8.

Figure 9 shows the variation of voltage (V) and power (P) with frequency ϕ for amplitude of excitation $\Gamma = 2$ and 4. One may observe that when Γ is decreased from 4 to 2, keeping the other parameters (ν, R_l) constant, the stable nontrivial (N-T) branch for $\phi < 4$ disappears. Also, the trivial unstable zone broadens for the higher amplitude of excitation and HB point gets shifted toward negative detuning from $\phi = 4.014$ to $\phi = 4.007$. The voltage output increases for a higher Γ value. For example, the output voltage increases from 1.13 V to 1.32 V and power increases from 2.55 mW to 3.45 mW at a particular value of $\phi =$

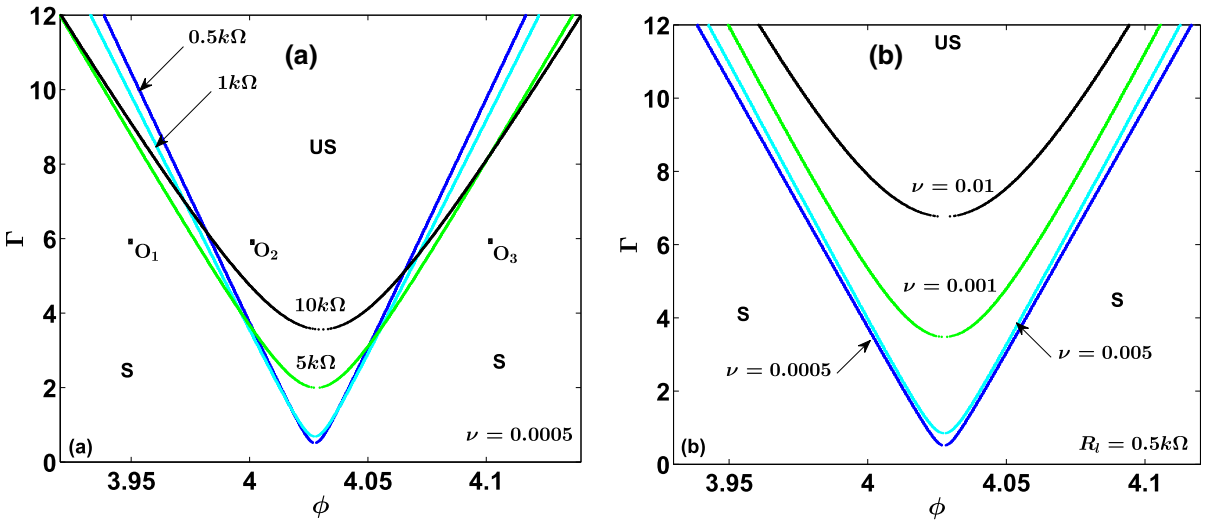

Fig. 3 Instability plot with **a** variation in load resistance $R_l = 0.5, 1, 5, 10$ kΩ for $\nu = 0.0005$ and **b** variation in damping parameter ν with $R_l = 0.5$ kΩ

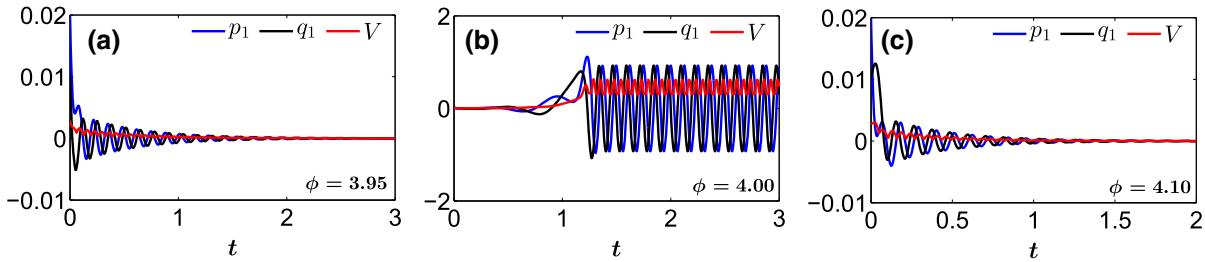

Fig. 4 Time response corresponding to the points O_1(3.95,6), O_2(4.00,6), and O_3(4.10,6)

4.050. For $\phi < 3.969$, the energy harvesting is possible in the case of $\Gamma = 4$, which depends on the initial conditions since the trivial branch is also stable for the mentioned zone of frequency. The N-T stable and unstable branches follow similar trends for positively tuned cases, and voltage increases with an increase in ϕ.

Figure 10 shows the frequency response curve for parameters $\nu = 0.0005$ and $\Gamma = 4$ with the variation in load resistance $R_l = 0.1, 0.5, 1, 2$ kΩ. It is observed that the voltage and power increase significantly as R_l increases which shows that the load resistance plays an important role in achieving an optimum power output. Here, at $\phi = 4.5$, a voltage of 0.77, 3.8, 7.77, and 15.3 V with corresponding power of 5.9, 29.5, 58.9, and 117 mW is achievable as the load resistance increases from $R_l = 0.1$ kΩ to $R_l = 2$ kΩ.

In this case, the unstable trivial frequency zone remains fixed ($4.001 < \phi < 4.054$, $\Delta\phi = 0.053$) and stable nontrivial branches for frequencies $\phi < 4.001$ disappear (as shown in the inset of Fig. 10a, only showing stable trivial and stable nontrivial branches) for higher load resistance values $R_l > 1$ kΩ.

Figure 11 shows the variation of voltage and power with frequency when damping parameter (ν) of the system increases from 0.0005 to 0.005 (for $\Gamma = 10$ and $R_l = 0.5$ kΩ). The unstable trivial zone decreases slightly ($\Delta\phi = 0.017$), and the nontrivial branch which lies in the negative detuning zone ($\phi < 3.813$, $\nu = 0.0005$) disappears as ν increases. However, the voltage and power reductions are not significant for a positively tuned system and both increase as the frequency of excitation increases. On the contrary, a significant change in the topology of the N-T branch of the solution is observed when damping parameter changes from 0.001 to 0.01, as shown in Fig. 12. The N-T stable and unstable branches in the positively tuned zone form a closed

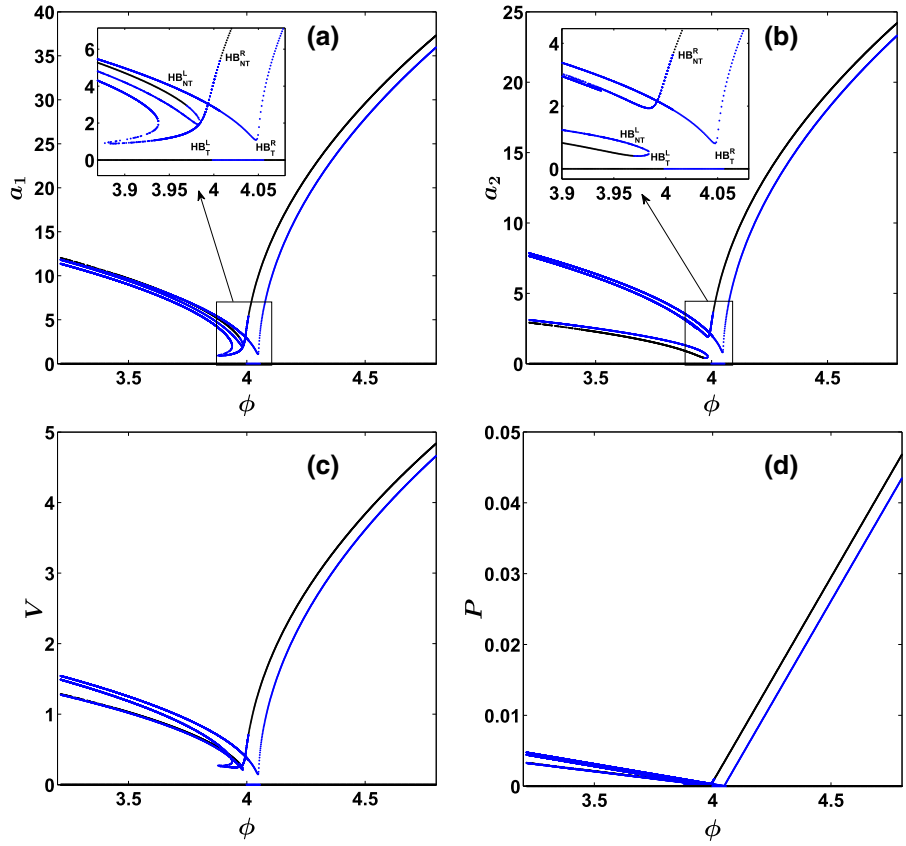

Fig. 5 **a**, **b** Frequency response plot, variation of **c** voltage and **d** power with frequency; for parameters $\nu = 0.0005$, $\Gamma = 4$, and $R_l = 0.5$ kΩ

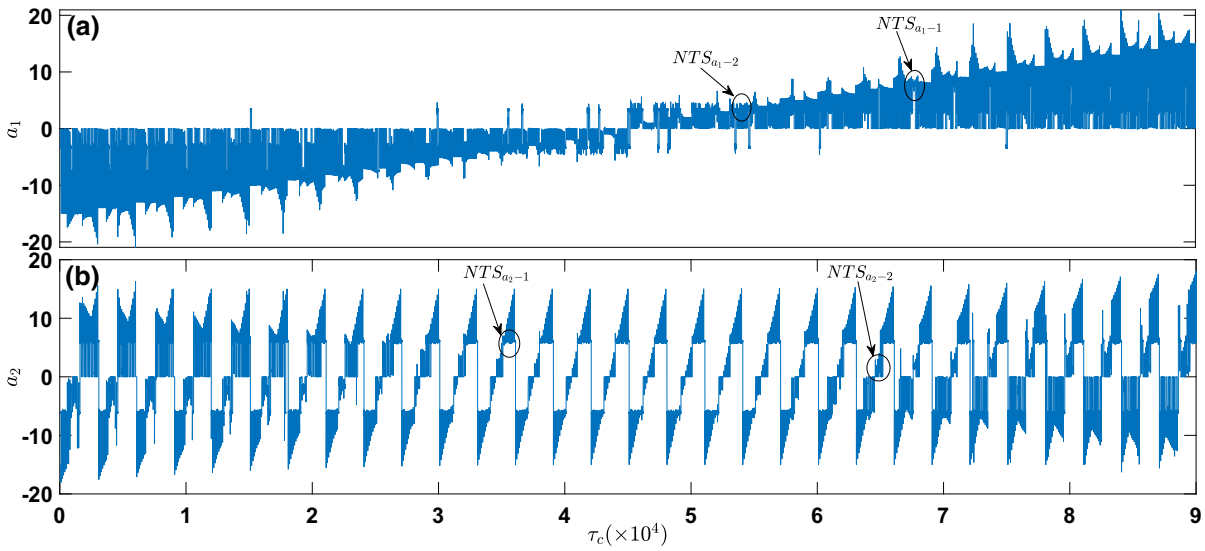

Fig. 6 Collection of time responses in a continuous time (τ_c), for different sets of initial conditions (a_1, a_2) while keeping $\gamma_1 = 3.78$ and $\gamma_2 = 4.97$ for **a** amplitude a_1 **b** amplitude a_2, at a particular frequency of excitation, $\phi = 3.7$; here, the system parameter is similar to that of Fig. 5, i.e., $\nu = 0.0005$, $\Gamma = 4$, and $R_l = 0.5$ kΩ

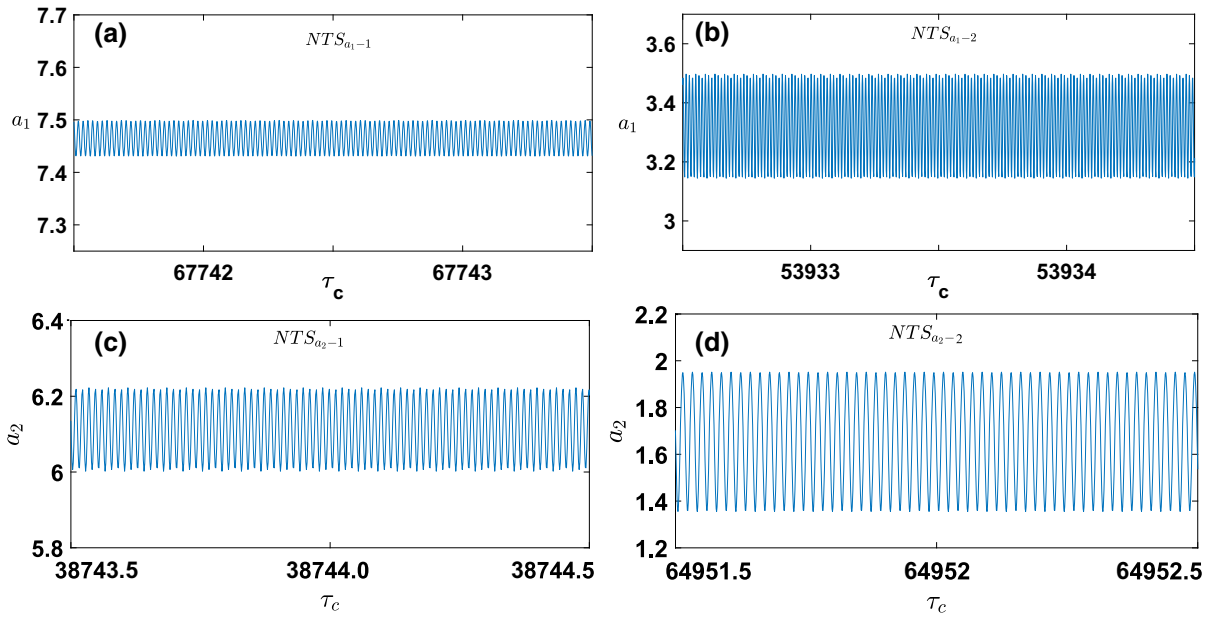

Fig. 7 Time responses of amplitudes a_1 and a_2 at selected ellipsoidal zones of **a** NTS_{a_1-1} **b** NTS_{a_1-2} **c** NTS_{a_2-1} and **d** NTS_{a_2-2}, from Fig. 6

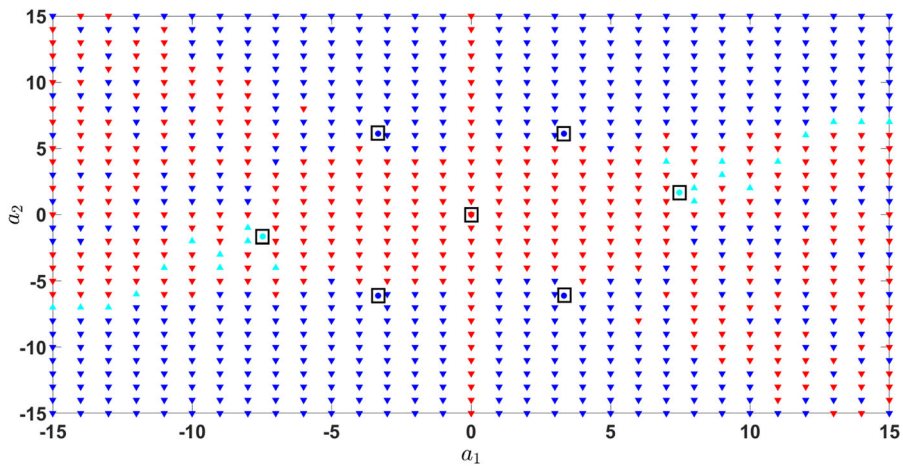

Fig. 8 The basin of attraction in $a_1 - a_2$ plane, while keeping γ_1 and γ_2 fixed

loop and stable branch loses stability at saddle node bifurcation point ($\phi = 4.01$, $\nu = 0.01$) where voltage output is found to be 0.54 V which is much reduced from 2.118 V for $\nu = 0.001$. Similar to the previous case here also the nontrivial branch, which lies in the negative detuning zone ($\phi < 3.883$, $\nu = 0.001$), disappears as ν increases and forms a close unstable N-T branch of solution. The trivial unstable zone gets reduced.

Variation of voltage (V) and power (P) with amplitude of harmonic excitation Γ is shown in Fig. 13 for ϕ=4 (tuned case) for different damping ratios $\nu = 0.001$ and 0.005, respectively, along with change in R_l. Both voltage and power increase, and the critical value of Γ shifts toward the higher side with R_l. The topology of the nontrivial branches of solution marginally changes as ν increases and the nature of stable nontrivial critical point changes from HB to saddle node bifurcation point. For example, in Fig. 13a $\Gamma_{\text{cr}} = 2.96$ ($V = 1.67$ V, at HB point) for nontrivial branch where $R_l = 1.5$ kΩ, while for higher damping $\nu = 0.005$ in Fig. 13c and $\Gamma_{\text{cr}} = 5.96$ ($V = 1.43$ V at SN point) for non-

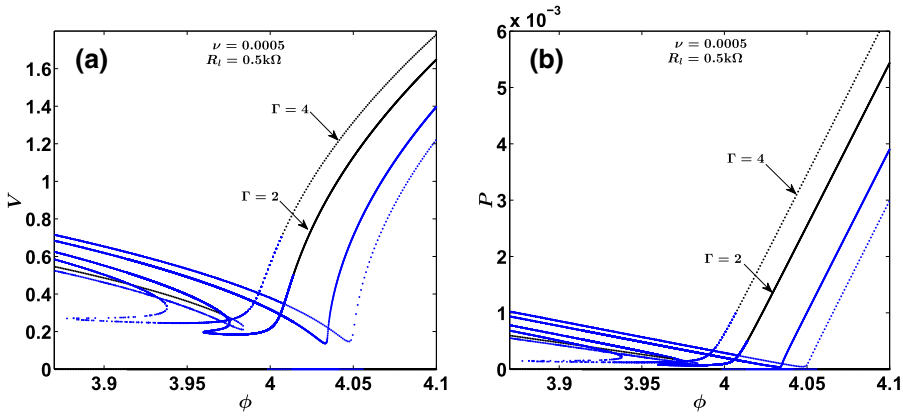

Fig. 9 Variation of **a** voltage, **b** power with frequency of excitation (ϕ) for system parameter $\nu = 0.0005$, $\Gamma = 2, 4$ and $R_l = 0.5$ kΩ

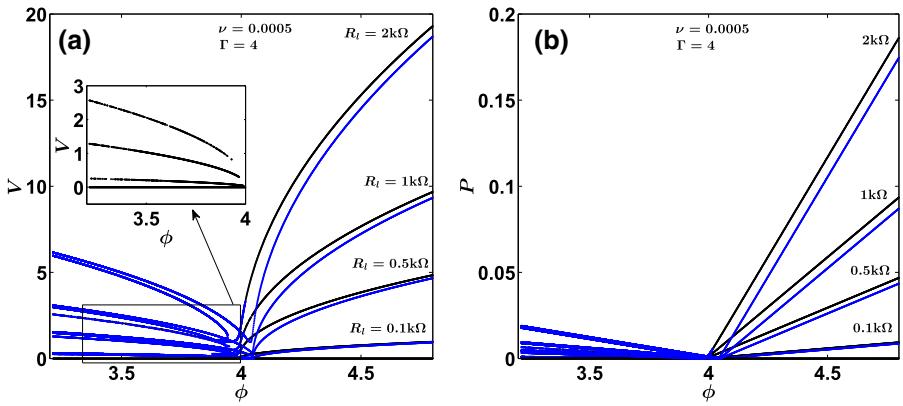

Fig. 10 Variation of **a** voltage and **b** power with frequency for $\nu = 0.0005$, $\Gamma = 4$ and load resistance $R_l = 0.1, 0.5, 1, 2$ kΩ

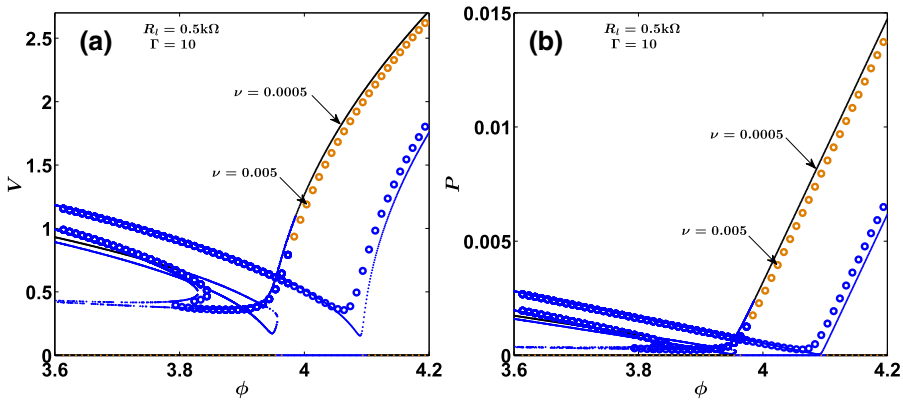

Fig. 11 The effect of damping parameter ν on **a** voltage and **b** power response for $\nu = 0.0005$ and $\nu = 0.005$ for $\Gamma = 10$, $R_l = 0.5$ kΩ

trivial branch where $R_l = 1.5$ kΩ. It is also observed that voltage and power are slightly reduced as damping increases and a higher damping ratio requires a higher critical value of Γ for harvesting purposes.

Considering $\nu = 0.001$, $\Gamma = 0$-10, and $R_l = 0.5$ kΩ for perfectly tuned ($\phi = 4$, $\sigma_1 = 0$), negatively tuned ($\phi = 3.9$), and positively tuned ($\phi = 4.1$) cases, variation of voltage and power with Γ is shown in Fig. 14. By Fig. 14(a,b), it has been observed that the voltage and power remain constant as Γ increases. The trivial state is stable in negatively and positively tuned cases, while it loses stability by Hopf bifurcation for a perfectly tuned case, as shown in Fig. 14c. The voltage and power increase as Γ increases for perfectly and positively tuned cases; however, the values are higher for the positively tuned case. The unstable nontrivial branch disappears as the frequency is tuned to perfect or kept to the positive side.

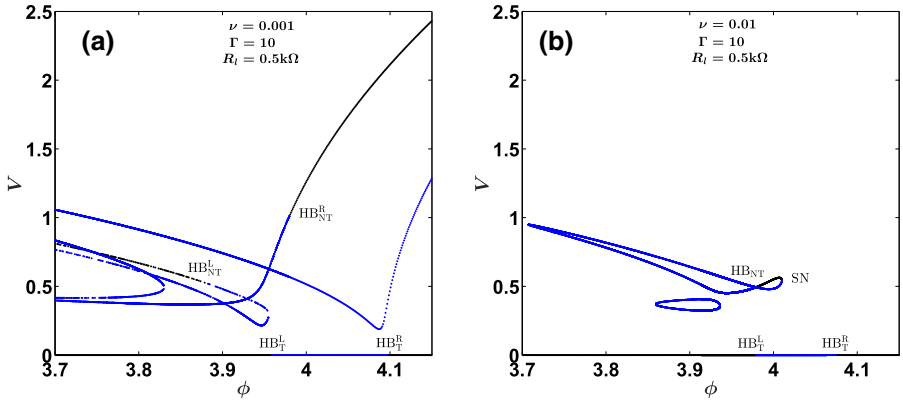

Fig. 12 The effect of damping on voltage response for **a** $\nu = 0.001$, **b** $\nu = 0.01$ for $\Gamma = 10$, $R_l = 0.5$ kΩ

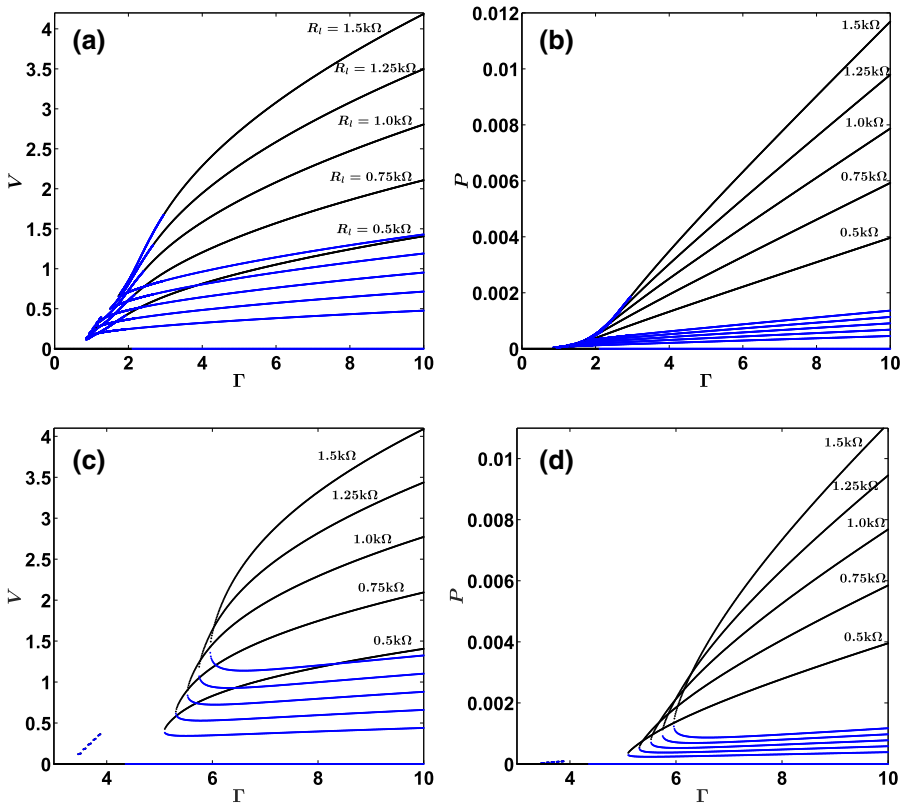

Fig. 13 Voltage and power variation with amplitude of excitation (Γ) for the system parameters $R_l = 0.5, 0.75, 1, 1.25, 1.5$ kΩ, $\phi = 4$ **a**, **b** $\nu = 0.001$ **c**, **d** $\nu = 0.005$

Voltage and power variation with load resistance (R_l) is shown in Fig. 15 for perfectly and positively tuned cases, and the effect of amplitude of excitation Γ on the output voltage and power is also observed. The trivial branch is unstable for the whole range of resistance variation for perfectly tuned case ($\phi = 4$), while it is completely stable for positively tuned case ($\phi > 4$). Output voltage increases with an increase in R_l up to a certain value and nontrivial stable branch loses stability by Hopf bifurcation at 1.545 kΩ ($\Gamma = 3$) and 2.295 kΩ ($\Gamma = 4$) as shown in Fig. 15a. Again for a range of $2.775 < R_l < 2.905$ and $3.870 < R_l < 4.045$ for $\Gamma = 3$ and $\Gamma = 4$, respectively, the stable branch appears and loses stability by SN bifurcation point. A similar trend is observed for positively tuned case ($\phi = 4.1$) except that continuous stable nontrivial branch exists and loses stability at SN bifurcation as R_l increases and voltage and power values are significantly higher than those of tuned case. The maximum

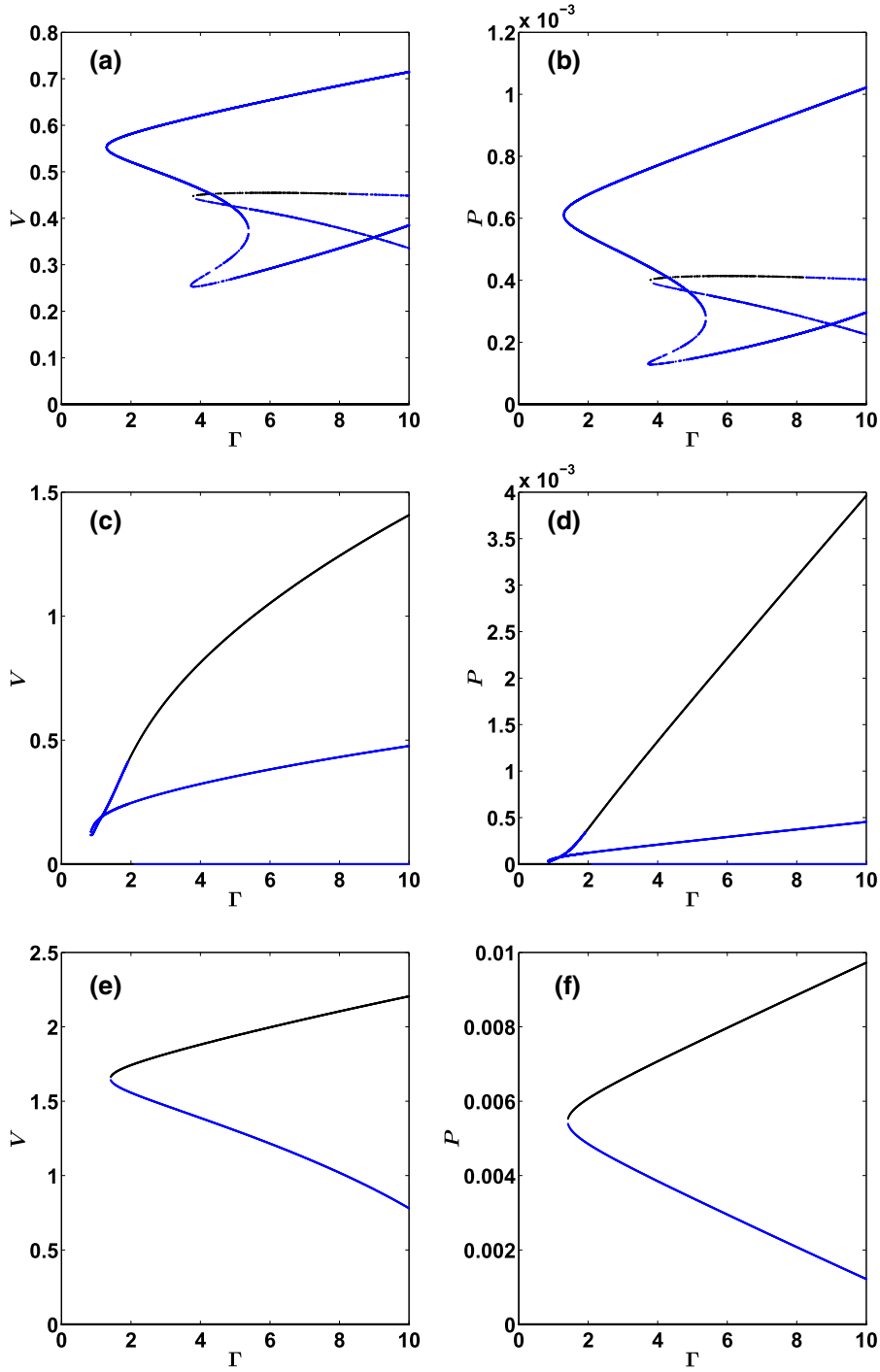

Fig. 14 Variation of voltage and power with amplitude of excitation (Γ) for the system parameters $\nu = 0.001$, $\Gamma = 0\text{-}10$, R_l=0.5 kΩ **a**, **b** negatively tuned $\phi = 3.9$ **c**, **d** perfectly tuned $\phi = 4.0$ and **e**, **f** positively tuned $\phi = 4.1$ case

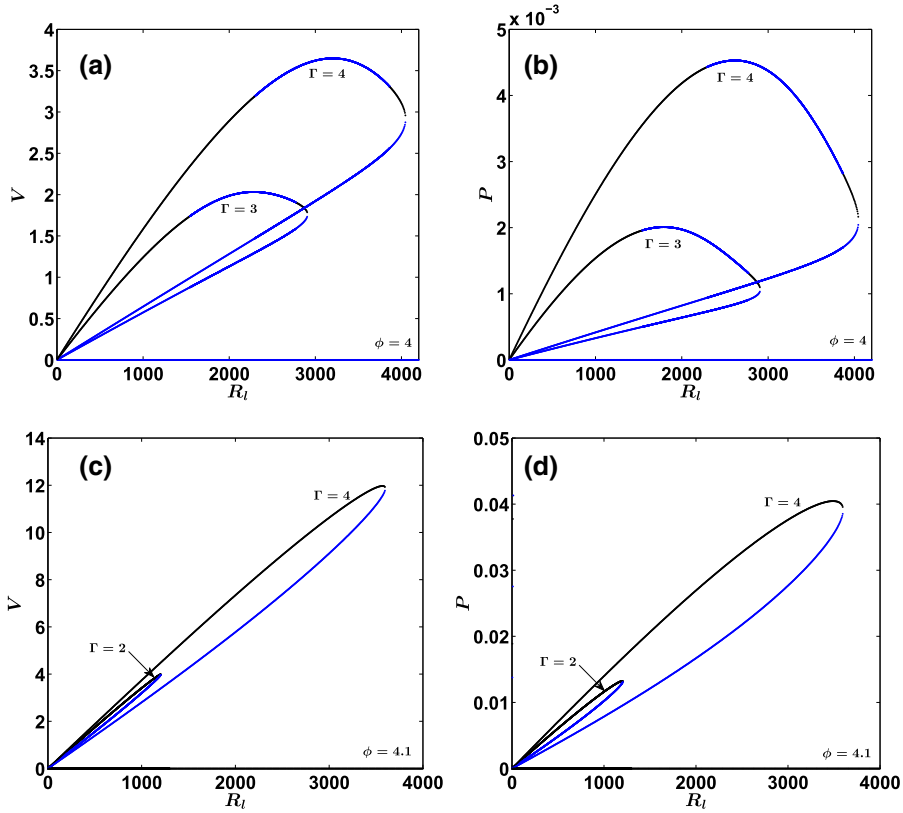

Fig. 15 Voltage and power variation with load resistance (R_l) for the system parameter $\nu = 0.001$ and **a**, **b** $\phi = 4$, $\Gamma = 3, 4$ **c**, **d** $\phi = 4.1$, $\Gamma = 2, 4$

value of power is found to be 40.46 mW at $R_l = 3.485$ kΩ and $\Gamma = 4$ as shown in Fig. 15d.

5 On achieving the internal resonance of 1:3

In the present energy harvester, the material properties of the substrate are considered from the work of Zavodney and Nayfeh [43]. However, the possibility of achieving the required commensurate frequency ratio of 1:3 by considering different values of system parameters, i.e., geometric (L_s, t_s, β, μ) and material properties (E_s), is explored in this section.

The effect of the distance of arbitrary mass (β) from the fixed end on frequency ratio $\frac{\omega_2}{\omega_1}$ is shown in Fig. 16, with a change in mass ratio (μ) and beam length (L_s). As the mass ratio increases, the frequency ratio becomes closer to the required value 3. A discontinuity is observed near $\beta = 2.72$, which remains invariant to μ but changes with a change in L_s value. This causes the frequency ratio $\frac{\omega_2}{\omega_1} > 3.4$ away from internal resonance phenomenon. For larger beam length, the discontinuity occurs at a lower value of β and vice versa. These curves are very much useful while considering the geometry and location of the arbitrary mass and its distance from the base in order to achieve or avoid the commensurate frequency ratio, which depends on the application.

In Fig. 17, variation in material property (Young's modulus of the beam, E_s) is plotted with frequency ratio $\left(\frac{\omega_2}{\omega_1}\right)$ with a change in substrate length (L_s) and thickness (t_s). As E_s increases, the ratio of frequencies gets reduced and an increase in the length of the beam causes the curve to shift at a higher frequency ratio side, as shown in Fig. 17a. However, as the thickness of the substrate (t_s) increases, the curve shifts toward the lower frequency ratio side. One may choose suitable values of system parameters to get the internal resonance of 1:3, for the present system, which is associated with the cubic and inertial nonlinearities due to the large deformation and an attached arbitrary mass.

In Fig. 18, the variation of mass ratio (μ) with frequency ratio $\left(\frac{\omega_2}{\omega_1}\right)$ is observed for different values of β, E_s, L_s, and t_s. As the mass ratio increases, the frequency ratio reduces. As the distance of attached mass (β) from the fixed end increases, the curve shifts toward lower frequency ratio side and around $\beta \approx 0.27$

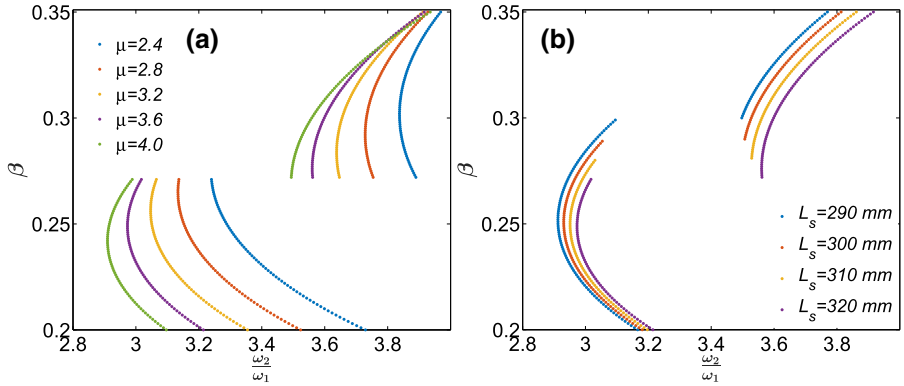

Fig. 16 The variation of distance of arbitrary mass (β) with frequency ratio ($\frac{\omega_2}{\omega_1}$) for different values of **a** mass ratio μ and **b** beam length L_s, while other geometric and material system parameters are same as mentioned in Table 1

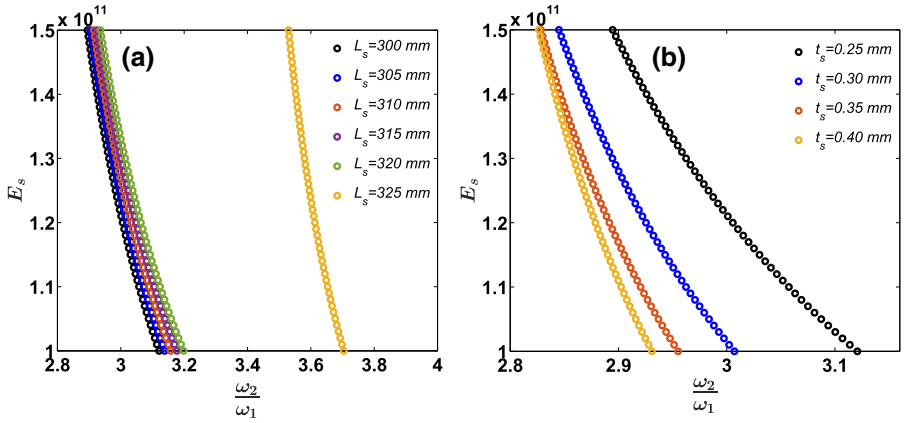

Fig. 17 The variation of Young's modulus of beam (E_s) with frequency ratio ($\frac{\omega_2}{\omega_1}$) for different values of **a** beam length, L_s, **b** substrate thickness t_s, while other parameters are the same as in Table 1

the frequency ratio switches to the higher ratio side as shown in Fig. 18a. Young's modulus in the range of 150 $< E_s <$ 210 is varied in Fig. 18b, and in every case one can get a frequency ratio of nearly 1:3. Higher E_s brings the frequency ratio at lower side, and this trend is similar for thickness t_s but opposite for larger beam length L_s values as shown in Fig. 18c, d, respectively.

6 Experimental findings with MFC patch

To validate the theoretical findings, experiments have been carried out by using an experimental setup which was previously used for comparing the results for principal parametric resonance condition [42]. The setup is shown in Fig. 19b, and the details of the setup can be found in the work of Garg and Dwivedy [48]. It may be noted that in the present case, the harvester has been excited at a frequency equal to the sum of the first two mode frequencies.

The material and geometric properties of the substrate and piezoelectric patch (MFC) used in this experiment are mentioned in Table 2. It may be noted that these properties are different from those in Garg and Dwivedy [48]. Here, MFC (M2814-P2, [49]) is used in place of PZT-5H, which is very brittle and may likely to be broken under combination parametric resonance case. The beam specimen is formed by using a laser cutting machine. The beam attached with the MFC patch and arbitrary mass is shown in Fig. 19a. The beam is attached to a slider crank mechanism-based shaker. The MFC patch is attached using 3M 465 film tape. Unlike the PZT ceramics, the MFC patch can be detached from the substrate for reuse purposes.

Figure 20 shows the voltage time response and corresponding FFT when the frequency of excitation is kept nearly 8 Hz, which is close to twice of the first natural frequency of the system. Here, the mass, its position along the beam, and load resistance values are taken as $m = 36$ gm, $\beta = 0.263$, and $R_l = 1000$ kΩ. Two frequency peaks are observed in Fig. 20b with frequencies 4.3 Hz and 8.6 Hz. The MFC patch is placed nearer to the fixed end of the beam (Table 2), which

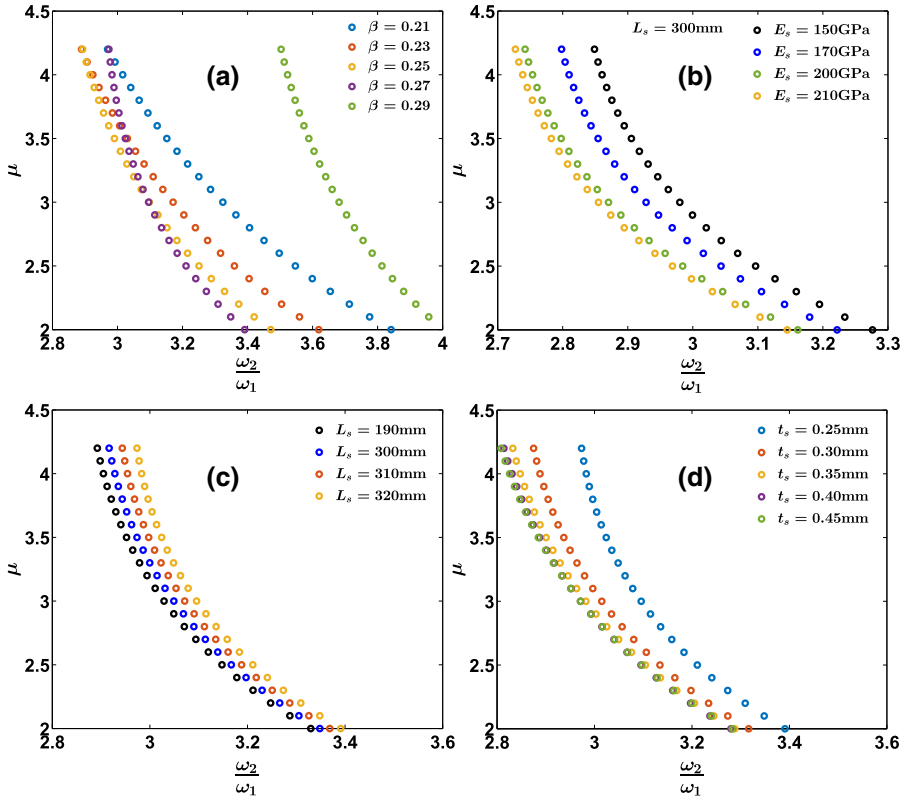

Fig. 18 The variation of mass ratio (μ) with frequency ratio $\left(\frac{\omega_2}{\omega_1}\right)$ for different values of **a** distance of arbitrary mass, β **b** Young's modulus of beam, E_s **a** beam length, L_s and **b** substrate thickness, t_s, while other parameters are the same as in Table 1)

Table 2 Material and geometric properties of substrate and piezoelectric patches

Property	Piezo-patch (M2814-P2)	Substrate
Young's modulus, GPa	$E_p = 15.86$	$E_b = 190$
Density, kg m^{-3}	$\rho_p = 5440$	$\rho_b = 7800$
Length, m	$L_p = 28 \times 10^{-3}$	$L_b = 190 \times 10^{-3}$
Width, m	$b_p = 14 \times 10^{-3}$	$b_b = 14 \times 10^{-3}$
Height, m	$t_p = 0.125 \times 10^{-3}$	$t_b = 0.25 \times 10^{-3}$
Permittivity, nFm^{-1}	$\hat{e} = 19.36$	–
Piezoelectric constant, Cm^{-2}	$e_{31} = -19.84$	–
L_1, m	10×10^{-3}	–
L_2, m	38×10^{-3}	–

leads to higher strain and, consequently, more output voltage around 5 V and power of 25 μW.

When the excitation frequency increases to near the second-mode frequency of the system, the voltage time response changes (shown in Fig. 21a) and higher frequencies dominate the time response which is visible in FFT (in 21b). The other parameters, i.e., m, β and R_l, are kept similar to that of the previous case. Here, it is observed that the output voltage reduces significantly. Two major frequency components are found to be 14.3 and 50 Hz, where the higher frequency is nearly three times the second-mode frequency of the system. It may be noted that by using the developed Eqs. (10) and (11) and the properties given in Table 2 the modal frequencies are found to be 4.58 and 14 Hz. This is matching very well with the experimentally obtained frequencies, as shown in Figs 20 and 21. Further, a positive detuning from 13 Hz leads to the multimodal

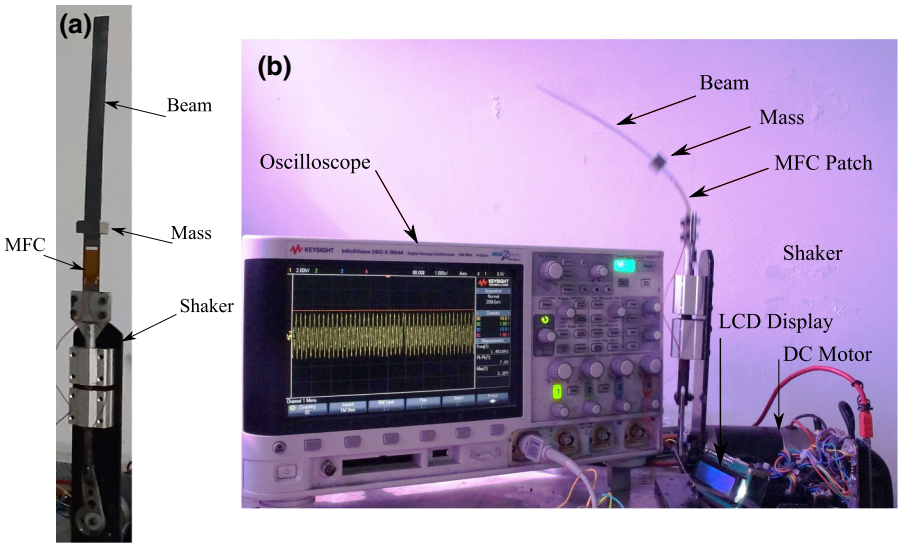

Fig. 19 **a** A vertical beam with unimorph MFC patch and an attached mass, **b** experimental setup

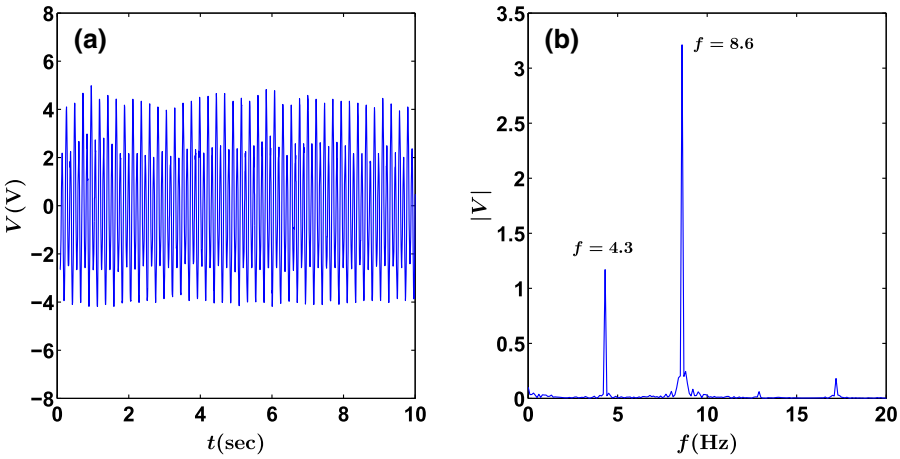

Fig. 20 **a** Voltage time response and **b** corresponding FFT, for parameters $m = 36$ gm, $\beta = 0.263$, $R_l = 1000$ kΩ and frequency of excitation is 8 Hz (principal parametric resonance condition with base acceleration of 16.4 m/s^2)

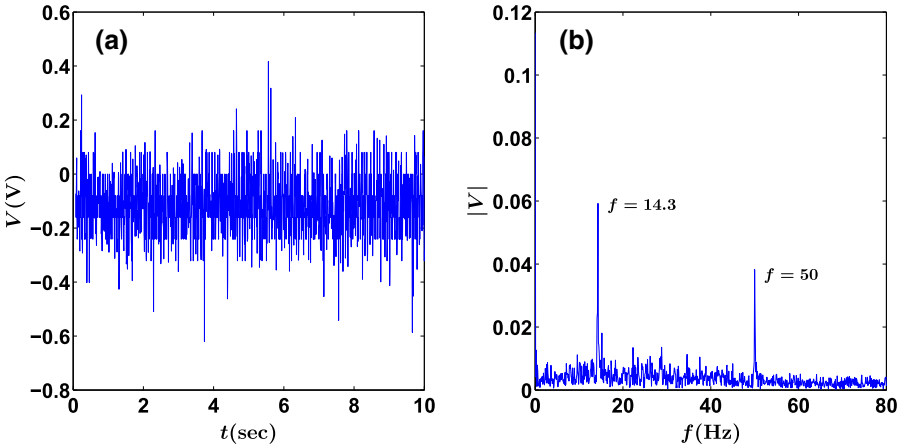

Fig. 21 **a** Voltage time response and **b** corresponding FFT, for parameters $m = 36$ gm, $\beta = 0.263$, $R_l = 1000$ kΩ. The frequency of excitation is 13 Hz which is around the combination of first two modal frequencies

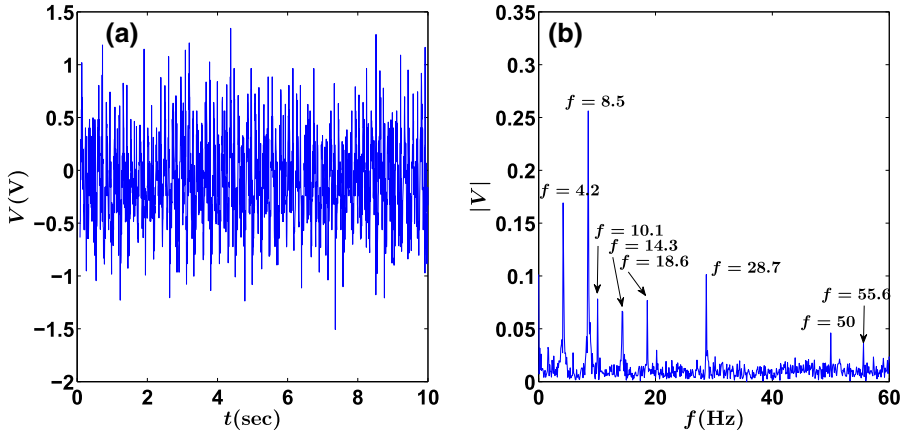

Fig. 22 **a** Voltage time response and **b** corresponding FFT, for parameters $m = 36$ gm, $\beta = 0.263$, $R_l = 1000$ kΩ and frequency of excitation is positively detuned to that of 13 Hz up to 17 Hz

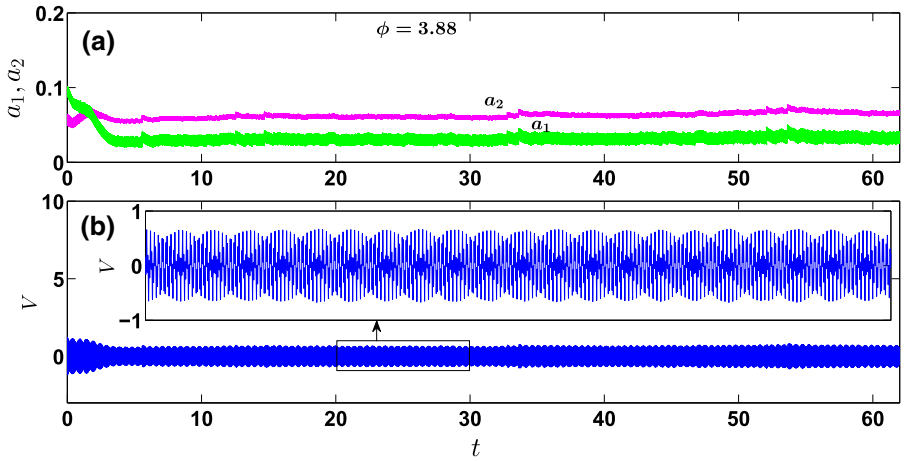

Fig. 23 Time response (using ode45 in MATLAB) for **a** amplitudes a_1 and a_2, **b** output voltage V, with system parameters same as in the experimental work (Fig. 22)

voltage time response (in Fig. 22a) with multiple frequency components in FFT as shown in Fig. 22b. The following frequency components in the FFT plot are observed: $f_1 = 4.3$ Hz, $f_2 = 14.3$ Hz, $f_2 - f_1 = 10.1$ Hz, $f_1 + f_2 = 18.6$ Hz, $2f_1 = 8.5$ Hz, $2f_2 = 28.7$ Hz. The higher output voltage is observed here as compared to the previous case where the excitation frequency is kept near to the second-mode frequency.

Figure 23 shows the amplitude and voltage time response obtained numerically solving the reduced Eqs. (20) to (23) using fourth-order Runge–Kutta method taking the system parameters as in the experimental work (Fig. 22). The frequency of excitation is taken as 17 Hz ($\phi = 3.88$) which is the combination of first two mode frequencies of the system, and the other parameters are kept same as that of used in the experimental findings, i.e., $m = 36$ gm, $\beta = 0.263$, $R_l = 1000$ kΩ (see Fig. 22). The numerically obtained output voltage is found to be in good agreement with the experimentally observed voltage. In Fig. 24, few specific frames are shown, which are related to the first, second, and combination of excited modes of the PEH system.

7 Conclusions

In this work, a harmonically base excited vertical cantilever beam with piezoelectric path and attached mass is used as an energy harvester. The mass is attached at a position such that the second modal frequency is thrice the fundamental frequency, and hence the system exhibits 1:3 internal resonance. The system is excited at a frequency nearly equal to the combination of the first and second modal frequencies. The nonlinear governing equation of motion, which is similar to that of a parametrically excited system with cubic nonlinearities, is derived and solved using the method of multiple scales. Initially, the instability regions have been plotted to obtain the range of frequencies for which the har-

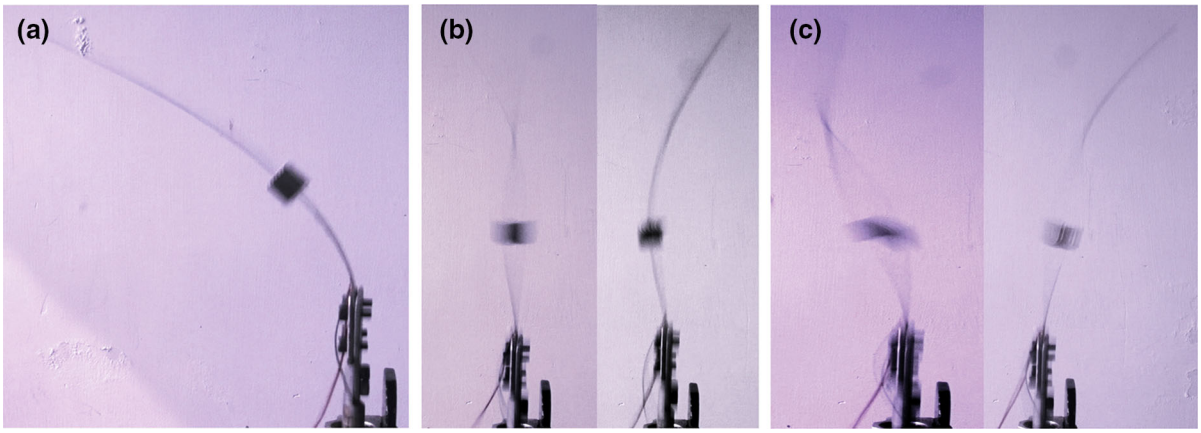

Fig. 24 **a** First mode (principal parametric resonance, see Fig. 20 for corresponding voltage time and FFT), **b** second mode (see Fig. 21 for corresponding voltage time and FFT), **c** combination of modes (combination parametric resonance, see Fig. 22 for corresponding voltage time and FFT)

vester can be effectively used for various system parameters such as the load resistance, excitation amplitude, excitation frequency, and damping. From these instability regions, it has been observed that there exists a critical value of the amplitude of the base excitation for different values of load resistance and damping, below which the harvester cannot be used as it leads to trivial state fixed-point response. Then, the frequency response curves have been plotted for the same parameters to obtain the voltage and power of the harvester. Time responses have been plotted to verify the instability regions and the frequency response curves, which are found to be in good agreement. From the frequency vs. power curves, it has been observed that there exist critical values of load resistance for optimum power generation. A modified form of the basin of attraction is also plotted which clearly shows the multiple stable fixed-point responses along with other periodic responses.

It has been observed that the present harvester will not only useful in energy extraction in the primary resonance zone but also the higher frequency zone of combination type ($\omega_1 + \omega_2$). Also, parametric excitation means a high deformation at the cost of very low excitation magnitude, which provides a high conversion rate of power with the only limitation of crossing the threshold limit of excitation magnitude necessary for transverse deflection of the vertical cantilever beam-based harvester.

For an external frequency of more than 13 Hz, the FFT of voltage time response for the PEH system shows multiple frequency components. Here, due to modal interactions between several participating modes, synchronous and sub-synchronous frequencies are observed, which are generally observed in the rotor-bearing system. The experimental findings are also compared with the numerically obtained amplitude and voltage time response for combination parametric resonance condition and is found to be in good agreement.

By suitably using different dimensions of the harvester, the load resistance, different types of the piezoelectric patch and base material and attached mass, one can extend the present analysis using the developed reduced equations to find the range of voltage and power of the harvester which can be used for a wide range of applications. This analysis of combination parametric resonance may be coupled with other resonance conditions for harvesting energy for a wider frequency range as the ambient response contains both low and high frequencies.

Funding Funding was provided by the Indian Institute of Technology Guwahati, India, as a research assistantship to the first author.

Compliance with ethical standards

Conflict of interest The authors declare that they have no conflict of interest.

Appendix A

$$h_{11} = \int_0^1 \tfrac{\rho(x)}{\rho_b A_b}\psi_n^2 \mathrm{d}x,$$
$$h_{12} = \int_0^1 \delta(x-\beta)\psi_n^2 \mathrm{d}x,$$
$$h_{13} = \int_0^1 \delta(x-\beta)\psi_{nx}^2 \mathrm{d}x,$$
$$h_{21} = h_{11},$$
$$h_{31} = \int_0^1 EI^*(x)\psi_n^2 \mathrm{d}x,$$
$$h_{32} = \int_0^1 \tfrac{\rho_b A_b EI^*(x)}{\rho(x)}\psi_n^2 \mathrm{d}x,$$
$$h_{33} = \int_0^1 \tfrac{\rho}{\rho_b A_b}(1-x)\psi_{nx}^2 \mathrm{d}x,$$
$$h_{34} = \int_0^1 \int_x^1 \delta(\xi-\beta)d\xi\,\psi_n^2 \mathrm{d}x,$$
$$h_{41} = \frac{1}{2}\int_0^1 EI^*(x)\psi_k\psi_{lx}\psi_{mx}\psi_n \mathrm{d}x,$$
$$h_{42} = \frac{1}{2}\int_0^1 \delta(x-\beta)EI^*(x)\psi_k\psi_{lx}\psi_{mx}\psi_n \mathrm{d}x,$$
$$h_{43} = 3\int_0^1 EI^*(x)\psi_{kx}\psi_{lxx}\psi_{mxxx}\psi_n \mathrm{d}x + \int_0^1 EI^*(x)\psi_{kxx}\psi_{lxx}\psi_{mxx}\psi_n \mathrm{d}x,$$
$$h_{51} = \int_0^1 \left\{\int_x^1 \left(\int_0^\xi \psi_{l\eta}\psi_{m\eta}d\eta\right)d\xi\right\} \tfrac{\rho(x)}{\rho_b A_b}\psi_{kx}\psi_{nx}\mathrm{d}x,$$
$$h_{52} = \left(\int_0^\beta \psi_{lx}\psi_{mx}\mathrm{d}x\right)\left(\int_0^\beta \psi_{kx}\psi_{nx}\mathrm{d}x\right),$$
$$h_{53} = \{\psi_{kx}\psi_{lx}\psi_{mx}\psi_{nx}\}_{x=\beta},\ \ h_{61} = h_{51}$$
$$h_{62} = \int_0^1 \tfrac{1}{2}\tfrac{\rho(x)}{\rho_b A_b}\psi_{kx}\psi_{lx}\psi_{mx}\psi_n \mathrm{d}x - \int_0^1 \tfrac{\rho(x)}{\rho_b A_b}\psi_{kx}\psi_{lxx}\left(\int_x^1 \psi_m d\xi\right)\mathrm{d}x$$
$$h_{63} = h_{52},\ \ h_{65} = 0.5h_{53},$$
$$h_{64} = \tfrac{1}{2}\{\psi_{kx}\psi_{lx}\psi_m\psi_{nx}\}_{x=\beta} - \psi_m(\beta)\int_0^\beta \psi_{kx}\psi_{lxx}\psi_n \mathrm{d}x$$
$$\zeta_n^* = \frac{ch_{21}}{2\epsilon\hbar_n\rho_b A_b\theta_1};\ \hbar_n = h_{11} + \mu h_{12} + J\lambda^2 h_{13},$$
$$\theta_n^2 = \frac{\kappa_n^4(h_{31}+\mu h_{32})}{\rho_b A_b L^4\hbar_n} - \frac{g(h_{33}+\mu h_{34})}{L\hbar_n},$$
$$F_{nm} = F_{nm}^*\frac{\Gamma}{\epsilon} = \frac{\Omega^2\Gamma z_r}{\epsilon\theta_1^2\hbar_n L}(h_{33}+\mu h_{34}),$$
$$\alpha_{klm}^n = \frac{\lambda^2}{\epsilon\rho_b A_b L^4\hbar_n\theta_1^2}\left\{\kappa_k^4(h_{41}+\mu h_{42}) + h_{43}\right\},$$
$$\beta_{klm}^n = \frac{\lambda^2}{\epsilon\hbar_n}\left\{h_{51}+\mu h_{52}+J\lambda^2 h_{53}\right\},$$
$$\gamma_{klm}^n = \frac{\lambda^2}{\epsilon\hbar_n}\left\{h_{61}-h_{62}+\mu(h_{63}-h_{64})+J\lambda^2 h_{65}\right\}$$
$$\alpha_{enj} = \alpha_{nj} + \beta_{en} + \gamma_{en},$$
$$\alpha_{nj} = \left\{\begin{matrix} 3\alpha_{nnn}^n & \text{for}\, j=n \\ 2(\alpha_{njj}^n + \alpha_{jjn}^n + \alpha_{jnj}^n) & \text{for}\, j\neq n \end{matrix}\right\}$$
$$\beta_{nj} = \left\{\begin{matrix} \omega_n^2\beta_{nnn}^n & \text{for}\, j=n \\ 2\omega_j^2\beta_{njj}^n & \text{for}\, j\neq n \end{matrix}\right\}$$
$$\gamma_{nj} = \left\{\begin{matrix} -3\omega_n^2\gamma_{nnn}^n & ;\, j=n \\ -2\left\{\omega_j^2\left(\gamma_{jnj}^n+\gamma_{njj}^n\right)+\omega_n^2\gamma_{jjn}^n\right\} & ;\, j\neq n \end{matrix}\right\}$$
$$Q_1^* = \alpha_{121}^1 + \alpha_{211}^1 + \alpha_{112}^1 + \omega_1\omega_2\left(\beta_{121}^1+\beta_{112}^1\right) - \omega_1^2\beta_{211}^1 - \left\{\omega_1^2\left(\gamma_{211}^1+\gamma_{121}^1\right)+\omega_2^2\gamma_{112}^1\right\},$$
$$Q_2^* = \alpha_{111}^1 - \omega_1^2\left(\beta_{111}^1+\gamma_{111}^1\right).$$

Other parameters are defined as follows:

$$z_r = 1\,\mathrm{mm},\ \ c = 1\,\mathrm{Ns-mm^{-2}},\ \ \mu = 3.6,$$
$$J = 0.0366,\ \ \beta = 0.27,\ \ \lambda = 0.1$$
$$\kappa_1 = 1.791,\ \ \kappa_2 = 3.244,\ \ \epsilon = 0.001,\ \ \omega_1 = 1,$$
$$\omega_2 = 3.013$$
$$\alpha_{\mathrm{e}11} = -9.306,\ \ \alpha_{\mathrm{e}12} = 9.312,\ \ \alpha_{\mathrm{e}21} = 60.12,\ \ \alpha_{\mathrm{e}22} - 255.7$$
$$f_{11} = 0.033,\ \ f_{12} = 0.0124,\ \ f_{21} = 0.0358,$$
$$f_{22} = 0.0852$$
$$Q_1^* = -10.12,\ \ Q_2^* = -37.4,\ \ \zeta_1 = 3.126\tfrac{\nu}{\epsilon},$$
$$\zeta_2 = 1.267\tfrac{\nu}{\epsilon}.$$

References

1. Meindl, J.D.: Low power microelectronics: retrospect and prospect. Proc. IEEE **83**(4), 619–635 (1995)
2. Beeby, S., White, N.M.: Energy Harvesting for Autonomous Systems. Artech House, Norwood (2010)
3. Priya, S., Inman, D.J.: Energy Harvesting Technologies, vol. 21. Springer, New York (2009)
4. Challa, V.R., Prasad, M.G., Fisher, F.T.: A coupled piezoelectric-electromagnetic energy harvesting technique for achieving increased power output through damping matching. Smart Mater. Struct. **18**(9), 095029 (2009)

5. Yan, Z., Abdelkefi, A., Hajj, M.R.: Piezoelectric energy harvesting from hybrid vibrations. Smart Mater. Struct. **23**(2), (2014)
6. Yang, W., Towfighian, S.: A hybrid nonlinear vibration energy harvester. Mech. Syst. Signal Process. **90**, 317–333 (2017)
7. Anton, S.R., Sodano, H.A.: A review of power harvesting using piezoelectric materials (2003–2006). Smart Mater. Struct. **16**(3), (2007)
8. Cook-Chennault, K.A., Thambi, N., Sastry, A.M.: Powering MEMS portable devices: a review of non-regenerative and regenerative power supply systems with special emphasis on piezoelectric energy harvesting systems. Smart Mater. Struct. **17**(4), (2008)
9. Erturk, A., Hoffmann, J., Inman, D.J.: A piezomagnetoelastic structure for broadband vibration energy harvesting. Appl. Phys. Lett. **94**(25), 254102 (2009)
10. Mann, B.P., Sims, N.D.: Energy harvesting from the nonlinear oscillations of magnetic levitation. J. Sound Vib. **319**(1–2), 515–530 (2009)
11. Arrieta, A.F., Hagedorn, P., Erturk, A., Inman, D.J.: A piezoelectric bistable plate for nonlinear broadband energy harvesting. Appl. Phys. Lett. **97**(10), 104102 (2010)
12. Ferrari, M., Ferrari, V., Guizzetti, M., Andò, B., Baglio, S., Trigona, C.: Improved energy harvesting from wideband vibrations by nonlinear piezoelectric converters. Sens. Actuators A **162**(2), 425–431 (2010)
13. Stanton, S.C., McGehee, C.C., Mann, B.P.: Nonlinear dynamics for broadband energy harvesting: investigation of a bistable piezoelectric inertial generator. Physica D **239**(10), 640–653 (2010)
14. Masana, R., Daqaq, M.F.: Electromechanical modeling and nonlinear analysis of axially loaded energy harvesters. J. Vib. Acoust. **133**(1), 011007 (2011)
15. Friswell, M.I., Ali, S.F., Bilgen, O., Adhikari, S., Lees, A.W., Litak, G.: Non-linear piezoelectric vibration energy harvesting from a vertical cantilever beam with tip mass. J. Intell. Mater. Syst. Struct. **23**(13), 1505–1521 (2012)
16. Triplett, A., Quinn, D.D.: The effect of non-linear piezoelectric coupling on vibration-based energy harvesting. J. Intell. Mater. Syst. Struct. **20**(16), 1959–1967 (2009)
17. Daqaq, M.F., Masana, R., Erturk, A., Quinn, D.D.: On the role of nonlinearities in vibratory energy harvesting: a critical review and discussion. Appl. Mech. Rev. **66**, 040801 (2014)
18. Nayfeh, A.H., Lacarbonara, W., Chin, C.-M.: Nonlinear normal modes of buckled beams: three-to-one and one-to-one internal resonances. Nonlinear Dyn. **18**(3), 253–273 (1999)
19. Cao, J., Zhou, S., Inman, D.J., Chen, Y.: Chaos in the fractionally damped broadband piezoelectric energy generator. Nonlinear Dyn. **80**(4), 1705–1719 (2015)
20. Cartmell, M.: Introduction to Linear, Parametric, and Nonlinear Vibrations. Chapman and Hall, London (1990)
21. Nayfeh, A.H., Mook, D.T.: Nonlinear Oscillations. Wiley, New York (2008)
22. Thomsen, J.J.: Vibrations and Stability: Advanced Theory, Analysis and Tools. Springer Science & Business Media, Berlin (2013)
23. Daqaq, M.F., Stabler, C., Qaroush, Y., Seuaciuc-Osorio, T.: Investigation of power harvesting via parametric excitations. J. Intell. Mater. Syst. Struct. **20**(5), 545–557 (2009)
24. Abdelkefi, A., Nayfeh, A.H., Hajj, M.R.: Global nonlinear distributed-parameter model of parametrically excited piezoelectric energy harvesters. Nonlinear Dyn. **67**(2), 1147–1160 (2012)
25. Jia, Y., Yan, J., Soga, K., Seshia, A.A.: A parametrically excited vibration energy harvester. J. Intell. Mater. Syst. Struct. **25**(3), 278–289 (2014)
26. He, X.Q., Rafiee, M., Mareishi, S.: Nonlinear dynamics of piezoelectric nanocomposite energy harvesters under parametric resonance. Nonlinear Dyn. **79**(3), 1863–1880 (2015)
27. Yildirim, T., Zhang, J., Sun, S., Alici, G., Zhang, S., Li, W.: Design of an enhanced wideband energy harvester using a parametrically excited array. J. Sound Vib. **410**, 416–428 (2017)
28. Mam, K., Peigney, M., Siegert, D.: Finite strain effects in piezoelectric energy harvesters under direct and parametric excitations. J. Sound Vib. **389**, 411–437 (2017)
29. Nayfeh, A.H., Balachandran, B.: Modal interactions in dynamical and structural systems. Appl. Mech. Rev. **42**(11), 175–202 (1989)
30. Nayfeh, A.H., Ibrahim, R.A.: Nonlinear interactions: analytical, computational, and experimental methods. Appl. Mech. Rev. **54**(4), B60–B61 (2001)
31. Franco, M., Damián, H.Z.: Internal resonance in a vibrating beam: A zoo of nonlinear resonance peaks. PLoS ONE **11**(9), 1–18 (2016)
32. Manevitch, L., Manevich, A.: The Mechanics of Nonlinear Systems with Internal Resonances. Imperial College Press, London (2005)
33. Vijayan, K., Friswell, M.I., Khodaparast, H.H., Adhikari, S.: Non-linear energy harvesting from coupled impacting beams. Int. J. Mech. Sci. **96**, 101–109 (2015)
34. Dwivedy, S.K., Kar, R.C.: Dynamics of a slender beam with an attached mass under combination parametric and internal resonances, part ii: Periodic and chaotic responses. J. Sound Vib. **222**(2), 281–305 (1999a)
35. Dwivedy, S.K., Kar, R.C.: Nonlinear dynamics of a cantilever beam carrying an attached mass with 1:3:9 internal resonances. Nonlinear Dyn. **31**(1), 49–72 (2003)
36. Jiang, W.A., Chen, L.Q., Ding, H.: Internal resonance in axially loaded beam energy harvesters with an oscillator to enhance the bandwidth. Nonlinear Dyn. **85**(4), 2507–2520 (2016)
37. Chen, L.Q., Jiang, W.A., Panyam, M., Daqaq, M.F.: A broadband internally resonant vibratory energy harvester. J. Vib. Acoust. **138**(6), 061007 (2016)
38. Harne, R.L., Sun, A., Wang, K.W.: Leveraging nonlinear saturation-based phenomena in an l-shaped vibration energy harvesting system. J. Sound Vib. **363**, 517–531 (2016)
39. Xu, J., Tang, J.: Multi-directional energy harvesting by piezoelectric cantilever-pendulum with internal resonance. Appl. Phys. Lett. **107**(21), 213902 (2015)
40. Rocha, R.T., Balthazar, J.M., Tusset, A.M., Piccirillo, V., Felix, J.L.P.: Nonlinear piezoelectric vibration energy harvesting from a portal frame with two-to-one internal resonance. Meccanica **52**(11–12), 2583–2602 (2017)
41. Yan, Z., Hajj, M.R.: Nonlinear performances of an autoparametric vibration-based piezoelastic energy harvester. J. Intell. Mater. Syst. Struct. **28**(2), 254–271 (2017)

42. Garg, A., Dwivedy, S.K.: Nonlinear dynamics of parametrically excited piezoelectric energy harvester with 1:3 internal resonance. Int. J. Non-Linear Mech. **111**, 82–94 (2019a)
43. Zavodney, L.D., Nayfeh, A.H.: The non-linear response of a slender beam carrying a lumped mass to a principal parametric excitation: theory and experiment. Int. J. Non-Linear Mech. **24**(2), 105–125 (1989)
44. Erturk, A., Inman, D.J.: A distributed parameter electromechanical model for cantilevered piezoelectric energy harvesters. J. Vib. Acoust. **130**(4), 041002 (2008)
45. Kar, R.C., Dwivedy, S.K.: Non-linear dynamics of a slender beam carrying a lumped mass with principal parametric and internal resonances. Int. J. Non-Linear Mech. **34**(3), 515–529 (1999)
46. Erturk, A., Inman, D.J.: Piezoelectric Energy Harvesting. Wiley, Hoboken (2011)
47. Dwivedy, S.K., Kar, R.C.: Dynamics of a slender beam with an attached mass under combination parametric and internal sesonances, Part I: Steady state response. J. Sound Vib. **221**(5), 823–848 (1999b)
48. Garg, A., Dwivedy, S.K.: Piezoelectric energy harvester under parametric excitation: a theoretical and experimental investigation. J. Intell. Mater. Syst. Struct. **31**(4), 612–631 (2019b)
49. MFC-M2814-P2. https://www.smart-material.com/MFC-product-P2.html, (2019)

Publisher's Note Springer Nature remains neutral with regard to jurisdictional claims in published maps and institutional affiliations.